Modal Response of a Transonic Fan Blade to Periodic Inlet Pressure Distortion

by

Robert M. Wallace

Thesis submitted to the Faculty of the
Virginia Polytechnic Institute and State University
in partial fulfillment of the requirements for the degree of

MASTER OF SCIENCE
in
Mechanical Engineering

APPROVED:

W.F. O'Brien, Committee Co-Chair	P.S. King, Committee Co-Chair
J.A. Kenyon, Committee Member	R.L. West, Committee Member

September 18, 2003
Blacksburg, Virginia

Keywords: distortion, HCF, modal response, periodic flow, transonic fan blade

Modal Response of a Transonic Fan Blade to Periodic Inlet Pressure Distortion

by

Robert M. Wallace

Committee Co-Chair: W.F. O'Brien

Committee Co-Chair: P.S. King

Mechanical Engineering

(ABSTRACT)

A new method for predicting forced vibratory blade response to total pressure distortion has been developed using modal and harmonic analysis. Total pressure distortions occur in gas turbine engines when the incoming airflow is partially blocked or disturbed. Distorted inlet conditions can have varying effects on engine performance and engine life. Short-term effects are often in the form of performance degradation where the distorted airflow causes a loss in pressure rise, and a reduction in mass flow and stall margin. Long-term effects are a result of vibratory blade response that can ultimately lead to high cycle fatigue (HCF), which in turn can quickly cause partial damage to a single blade or complete destruction of an entire compressor blade row, leading to catastrophic failure of the gas turbine engine. A better understanding and prediction of vibratory blade response is critical to extending engine life and reducing HCF-induced engine failures.

This work covers the use of finite element modeling coupled with computational fluid dynamics-generated pressure fields to create a generalized forcing function. The first three modes of a low-aspect-ratio, transonic, first stage blade of a two-stage fan were examined. The generalized forcing function was decomposed to the frequency domain to identify the dominant harmonic magnitude present, as well as other contributing harmonics. An attempt to define the relationship between modal force with varying total

pressure distortion levels produced a sensitivity factor that describes the relationship in the form of a simple multiplier. A generalized force was applied to the blade and varied harmonically across a frequency range known to contain the first natural frequency. The mean rotor stress variation was recorded and compared to experimental results to validate the accuracy of the model and verify its ability to predict vibratory blade response accurately.

Acknowledgements

I would like to thank my graduate committee for serving in this capacity. A special thanks is deserved by my co-chairmen, Dr. O'Brien and Dr. King. Dr. O'Brien for initially accepting me into the Turbo Lab and giving me the opportunity to work on a project that combined my two top interests, fluids and finite element analysis. Dr. King for acting as much more than a committee member and contributing so much on a daily basis just to get me through this program. I would also like to thank Dr. West and Dr. Kenyon for their vast knowledge without which I would have been lost. Dr. Rabe and the Compressor Research Facility at Wright Patterson Air Force Base also deserve thanks for funding this project and providing the data required for the study.

I couldn't have made it without the friendship of everyone in the Turbo Lab, the air conditioner, and the maintenance men that installed the drop ceiling to further separate the lab from the university steam pipes which has made this windowless cave more tolerable. All those that follow should be grateful. Thanks to John, Mac, Kevin, Joe, Mano, Katie, Melissa, Matthew, Darius, and Mike for their help in making this the best and most enjoyable lab in the department.

I would also like to thank all my friends and family outside of the academic world for their guidance and support, specifically my parents and grandparents. I've been blessed to have parents as supportive as Ernie and Dianne Wallace that have allowed me to pursue anything I want and supported every decision I've made along the way, even if it took some convincing. In addition, my grandparents, Bob and Anne Wallace for supporting me in every way possible, acting as close to a second set of parents as one could have. This accomplishment as well as all those preceding has been a direct result of their love and support.

Table of Contents

Table of Figures

Table of Tables

1 Introduction

The assumption that the airflow at the inlet of axial turbomachinery is uniform has widely been accepted historically. In the early years of turbomachinery design, this assumption was acceptable and more useful than it is today for a number of reasons. As the performance of modern aircraft and their engines increase, the rotating blades of the engine are required to withstand more loading and in varying directions, both sometimes changing very rapidly, pushing ever closer to the material strength and fatigue limits.

High G maneuvers, such as aggressive turning, often cause the inlet flow to be non-uniform as it must enter the engine at a sharp angle to the axis of rotation as the aircraft turns. In addition, traveling in the wake of other aircraft and firing wing-mounted weapons can cause disturbances in the airflow. Vertical take-off and landing (VTOL) aircraft present yet another scenario for ingesting a non-uniform flow as exhaust gases are often mixed with cooler atmospheric air as they wash off the ground and are pulled back into the engine (see Figure 1-1). These disturbances, be it a change in total pressure or total temperature, are referred to as inlet distortions. These distortions by the nature of their source can be highly unpredictable and often changing throughout an aircraft's flight envelope.

A second source of inlet distortions can be the result of the engine's nacelle design or other obstructions related to the aircraft structure. As an example, a support strut, an S-shaped inlet duct, or the engine inlet's proximity to other exterior features of the aircraft can cause a non-uniform flow to enter the engine. Distortion caused by objects in a fixed location related to the engine's inlet presents a more static or constant disruption in the airflow. These quasi-static distortion patterns can be modeled and studied much more easily and are the focus of this research.

Inlet distortions can cause many problem areas to arise, from short-term performance degradation to long-term structural degradation. Short-term effects include loss of pressure rise and a reduction in mass flow, which can ultimately lead to a reduction of stall margin. These short-term effects have been studied a great deal and are often the result of the dynamic inlet distortions mentioned above (see Figure 1-2).

Figure 1-1: The AV-8B Harrier on take off is an example of hot exhaust gases mixing with cooler atmospheric air [www.globalsecurity.com].

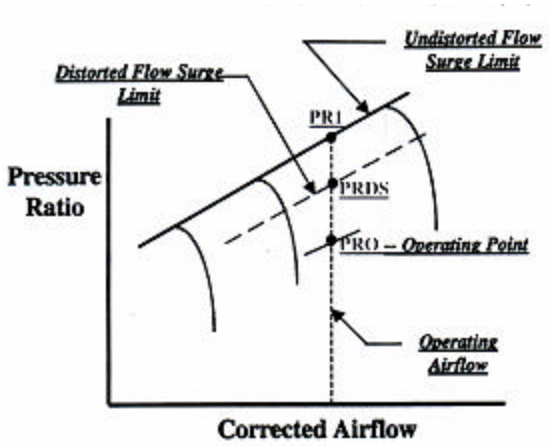

Figure 1-2: Compressor map showing the loss in surge limit caused by a distorted inlet flow [ARP-1420, 2002].

The long-term effects, however, are caused by repeated exposure to the dynamic inlet distortions or, more likely, the result of operating in the presence of a quasi-static distortion pattern.

By definition, all turbomachines are mechanical devices that transfer power by rotating blades around an axle or spindle, as the word *turbo* comes from the Latin meaning "to rotate." It is this fundamental mode of operation that makes all distortions

appear periodic in nature as seen by the fan or compressor blades of a gas turbine as they sweep past the section of distorted airflow. For example, if a single strut spanning the entire diameter of the inlet is partially blocking the airflow, then a change in the total pressure as seen by the fan blades will occur twice per revolution. Divide this by the time it takes to complete one revolution, and what was a constant pressure distortion in the stationary frame of reference becomes a time-dependent impulse in the rotating frame of reference at a certain frequency determined by the speed of rotation.

This periodic change in total pressure causes varying blade loading. If the frequency at which the blade load changes coincides with one of the natural frequencies of the blade, a very dangerous situation can occur, leading to rapid blade failure due to high cycle fatigue. High cycle fatigue (HCF) is defined as metal fatigue that results in cracking or fracture from a large number of stress cycles well below the yield strength of the material, and is associated with fatigue lives greater than about 10^4 to 10^5 cycles. At first inspection this may seem like a very high number of cycles for a lower limit. However consider the single strut mentioned above. If the blade is subjected to this excitation at 10,000 RPM, not an uncommon operational speed for today's engines, then each blade will be cycled 10^5 times in just five minutes as it is excited twice per revolution. Doubling the number of excitations per revolution reduces the time by one-half, and so forth. Now, assume this excitation at approximately 333 Hz coincides with one of the natural frequencies of the blade. This means that the blade loading changes concurrently with blade deflection in a way that amplifies blade bending to the point of catastrophic failure. This type of blade failure can take place in a much shorter time period, on the order of seconds under the right conditions.

The risk of catastrophic failure occurring so quickly has lead to much time, energy, and money spent on testing varying distortion patterns placed at the inlet (see Figure 1-3) as previous research has shown that total pressure distortion is a dominant HCF driver [Manwaring et al, 1997].

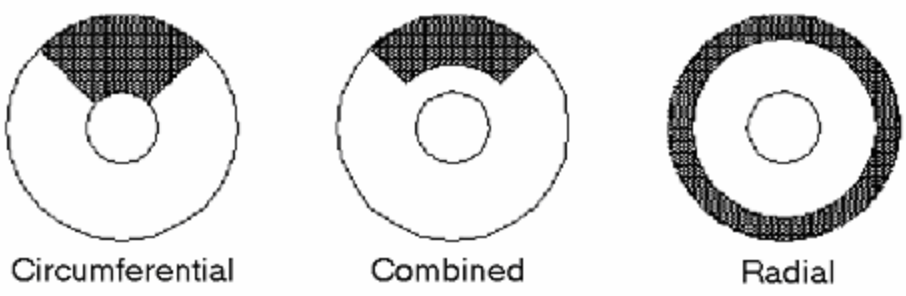

Figure 1-3: Examples of typical screens used to produce pressure distortions during testing [Eddy, 2001].

If a mathematical model representing the blade and how it responds to total pressure distortion could be developed, much time and money could be saved by partially eliminating such extensive testing. This provides the motivation for my research.

The goals of my research are as follows: (1) create an accurate finite element (FE) model of the ADLARF fan blade for eigenvector extraction; (2) identify dominant engine order modal force magnitudes based on coupling computational fluid dynamics (CFD)-generated total pressure distortion and FE generated eigenvectors; and (3) determine the relationship between the magnitude of the modal force and the total pressure distortion level used to drive the system. The modal force represents the magnitude of the generalized forcing function used to drive a model of the ADLARF fan blade for a given mode. If a relationship between the level of total pressure distortion present and the response of the fan blade can be identified through the use of a simplified model, perhaps large savings from multiple resources can be realized.

2 Literature Review

The idea of non-uniform inlet conditions leading to reduced compressor performance is not new and has been the subject of many experimental and analytical studies dating back to the 1950s. Most of this work has been concentrated around reductions in compressor performance in the form of reduced stall margins and pressure rise. This included many studies measuring, predicting and indexing various inlet distortions and will be discussed in this chapter. In recent years, a separate yet very much related area has been studied. The effects of blade response caused by forced vibration due to non-uniform inlet distortions has been studied with emphasis on compressor blade life due in part to HCF. The forced vibrations have lead to studying aeromechanical effects known as blade vibratory response. Studying blade vibratory response experimentally has proved difficult due to the speed at which the blade operates. Recent developments in computer modeling and computational ability have opened the door to CFD and finite element modeling (FEM) as viable analytical methods to accurately recreate and study blade vibratory response.

Despite significant gains made to date in understanding the effects of non-uniform inlet conditions, the need to further our understanding is ever present and even more so in the relatively new area of compressor aeromechanical response. A variety of modeling techniques, along with their successes and limitations, will be discussed in this chapter. Finally an introduction to a new attempt in modeling the aeromechanical effects and predicting blade vibratory response will be presented.

2.1 Inlet Pressure Distortion Effects on Compressor Performance and Blade Response

While many types of inlet distortions can occur, total pressure distortions are the focus of this research and therefore a timeline of studies on this topic will be presented. Reid [1969] performed a series of experiments using different inlet distortions and studied how

this affected the compressor's performance. His major contribution to the area of inlet distortion studies comes from his work to define what is known as the angle of spoiling. The spoiling angle is defined as the angular width of the low total pressure region. Using a varying spoiling angle Reid was able to show how the surge delivery static pressure varies accordingly, Figure 2-1 presents his findings. Notice how the area labeled "critical angle" defines a point in the spoiling angle range where little change in surge margin is present. Beyond this critical angle the surge delivery static pressure remains relatively constant. In addition, Reid was able to show that sub-dividing the area of spoiled flow has less effect on the peak pressure loss than one larger distorted sector does.

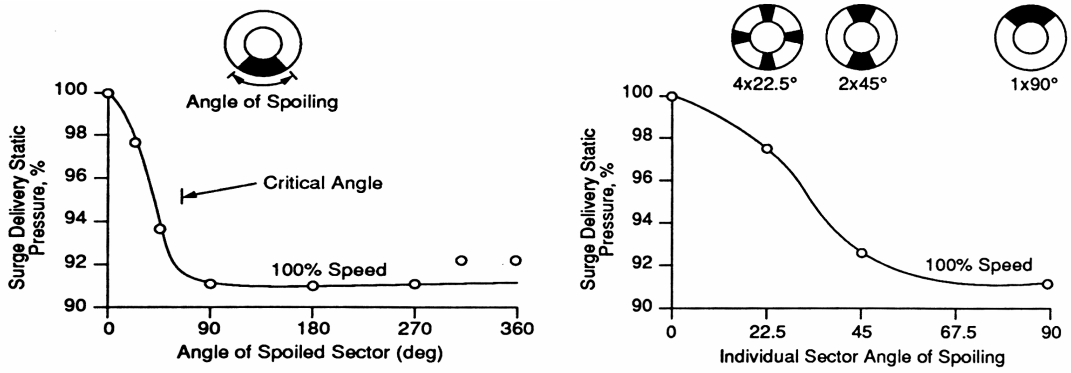

Figure 2-1: The effects of spoiled sector width on surge delivery static pressure [Reid, 1968].

Later, Danforth [1975] studied the effects of an inlet distortion on compressor stall margin and blade response. He examined several mechanisms that have the potential to reduce compressor stall margin and induce forced blade vibrations and concluded that the effects can be extremely different. While Reid showed large areas of distorted flow can adversely affect the static delivery pressure, Danforth showed that small regions of distorted flow that would be insignificant in Reid's study could generate large vibratory responses in both rotor and stator blades. In addition, Danforth noted that coupling a circumferential total pressure distortion that appears periodic to the passing blades can create severe blade vibrations if present at or near the natural frequency of the blade. The severity of the blade vibrations is directly related to the energy input which led Danforth to create a distortion index. This index has been used as an alert for

potential problems that exist in a blade design in the area of forced blade vibratory response.

Along the same time as Danforth, Peacock and Overli [1975] also used circumferential distortion to study the unsteady normal force at mid span of a lightly loaded low speed compressor. They used two different screen types to create the inlet distortions needed for their experiment. The first screen consisted of a sine wave distortion pattern where the screen porosity gradually changes over the circumference of the inlet. The second screen was comprised of sections of uniform screen porosity effectively creating a square wave input as seen by the passing rotor blades. As can be imagined, the results showed a more violent blade response to the square wave as the time rate of change in axial velocity was much greater than that of the sine wave. A correlation between the time rate of change in the axial velocity of the incoming air and the normal blade coefficient was theorized.

A year later Lecht and Weyer [1976] published their findings on a similar experiment conducted on both a subsonic and transonic compressor. Lecht and Weyer increased the number of blade force measurement locations taken relative to the low total pressure area. The results indicated that the blade experienced the maximum and minimum loads immediately after exiting and entering the spoiled area, respectively.

In the late 80s Datko and O'Hara [1987] continued testing a transonic compressor's response to seven different inlet total pressure distortion screens. To create a baseline case in which to compare the measured response with, two inlet configurations were tested with a "clean" designation, meaning no distortion screens were used. In addition, Datko and O'Hara used a compressor containing a blisk. The word blisk comes from the combination of the words "bladed disk" and indicates the blades are not fitted with traditional dovetail joints and instead are part of a monolithic piece of metal combining the hub and blades. The lack of dovetail joints greatly increases the strength of the rotor/blade system at the expense of severely reducing the mechanical damping present. As expected, the blisk underwent severe resonant stresses when exposed to inlet distortions. The major resonant stresses occurred at the first three natural modes of vibration where large deflections are common. The first stage compressor blade used for my research is also a blisk and the first three natural modes are studied.

In the progression of studies, Manwaring and Fleeter [1989,1990] introduced unsteady inlet flow conditions to the testing of a compressor rotor blade row. Steady loading was used while varying aerodynamic forcing functions were included in the distortion placed on the blade row. A steady 2-per-rev inlet distortion was placed in the flow while an unsteady simulated wind gust amplified the distortions. Measurements were taken to study the aerodynamic response, as well as the blade surface pressures. To better examine the forcing function as seen by the blades, the results were transferred to the frequency domain using Fourier decomposition. Not surprisingly, the 2-per-rev signal also known as the 2^{nd} engine order, or 2^{nd} harmonic, contained the largest magnitude and therefore was dominant. Higher harmonics of the 2^{nd} harmonic were present and gained magnitude with increasing gust magnitudes.

Later, Greitzer et al. [1994] further studied the effect that non-uniform inlet conditions have on both the aeromechanical excitation of a compressor and the overall stability of the compressor system. In addition to the forced response previously mentioned, Greitzer et al. examined flutter, a self excited aeromechanical instability. Possibly as part of the motivation to study these effects, it was noted that several hundred engine failures since the late 1960's had occurred in U.S. Air Force aircraft engines and mostly were attributed to high cycle fatigue (HCF) [Air Force Scientific Advisory Board, 1992]. Greitzer et al. suggested much work was needed for a better understanding of the stage-to-stage transfer of inlet distortions in multistage compressors, a research focus here at Virginia Tech. Ryman [2003] showed Volterra modeling is capable of predicting total pressure distortion transfer through compressor stages, the dominant driver of HCF, with limitations and requires further study. Secondly, Greitzer et al. also recommended further work in predicting the aerodynamic forcing functions that can cause blade excitation that can lead to HCF, which is related to my research in an attempt to model vibratory blade response to aerodynamic forcing functions.

2.2 Research Focused on Testing and Modeling Resonant Vibratory Response with Computer Modeling

Most recently and directly related to my research, Manwaring [1997] examined a low-aspect-ratio, transonic, first stage blade of a two stage fan with a series of experiments with the goal of characterizing aspects of distortion in order to create models to predict its effects. Manwaring tested two types of inlet flow distortions, a 3-per-rev and an 8-per-rev, using distortion screens. By mounting on-blade pressure transducers along with strain gages mounted at three positions on the blade, vibratory response was recorded for the unsteady blade loading. Special attention was shown to the areas of operation where the blade undergoes resonance, caused by exciting the blade near its natural frequency. Manwaring was able to test at these areas by constructing a Campbell diagram which identifies areas of probable vibratory problems. Wilfred Campbell [1924] developed a diagram that shows the natural frequency of a blade for various modes with multiple per-rev lines superimposed. Figure 2-2 shows Manwaring's Campbell Diagram with four blade modes lines and three per-rev lines, the 2-, 3-, and 8-per-rev. As can be seen in the diagram, the centrifugal force placed on the blade during operation increases the natural frequency at which the mode occurs by artificially stiffening the blade. Anywhere a mode line crosses a per-rev line, severe vibratory response is almost guaranteed as the distortion pattern and operation speed excited the blade at resonance.

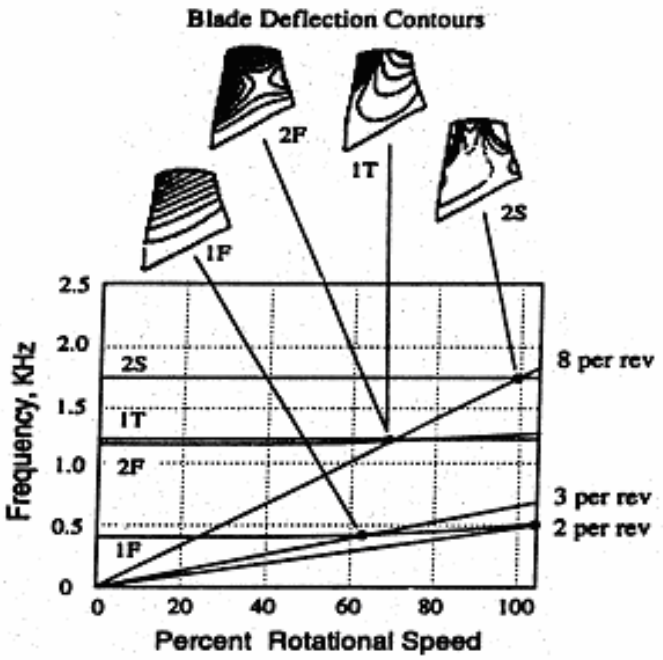

Figure 2-2: Campbell Diagram [Manwaring et al., 1997].

Hah et al. [1998] used Reynolds-averaged Navier-Stokes CFD code to model the same experiment studied by Manwaring. The inlet distortion pattern was modeled and used to predict the blade pressure profiles on both the pressure and suction side of the blade. Upon comparison, Hah's numerical solution successfully predicted the flow field to that found in the experiments. The pressure field generated by Hah's CFD was used in my research and in part made my research possible.

Using modal analysis to predict stresses in the blade due to vibratory response requires that the correct eigenvector must be used in calculations. This requires the correct mode shape used in modeling to match the actual mode being excited during engine operation and testing. This may seem trivial with the graphical display of a Campbell diagram to help the researcher determine which mode shape is present; however, what happens when two mode lines converge or cross has been a topic of debate.

Kenyon [1999] investigated a phenomenon called curve veering using computational and experimental techniques. Upon first inspection it appears that mode

lines simply cross with no special occurrences taking place. However, mathematical models have shown that when eigenvalues converge, the mode lines do not cross and instead the eigenvalues "repel" each other while abruptly swapping mode shapes. Kenyon showed through use of finite element modeling that a compressor blade over a range of speeds demonstrates that the interacting modes veer away from each other rather than cross while switching their respective eigenvalues. In his study, however, the interaction was not abrupt and took place over a large range of the compressor operating range. Figure 2-3 is a close up of converging mode lines from a finite element model over a short operational range, the dark solid portion of both lines indicating where the modes swap.

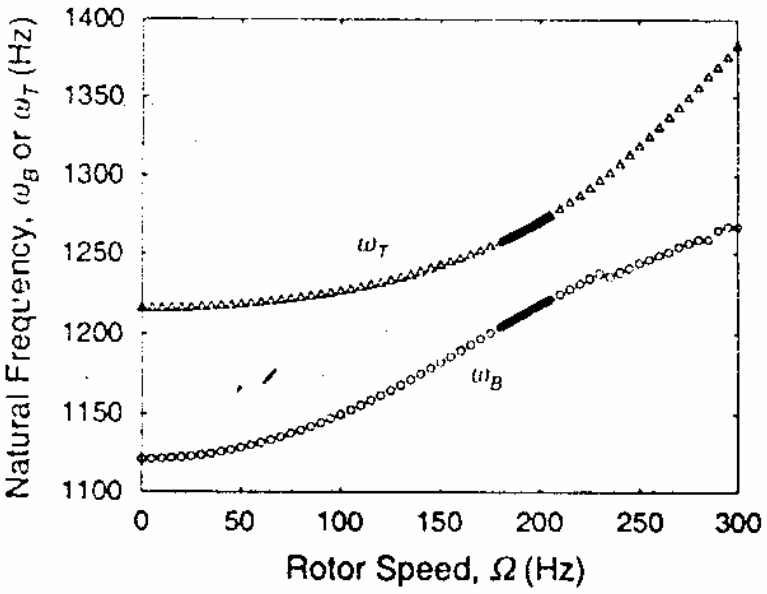

Figure 2-3: Sample of curve veering [Kenyon, 1999].

During the interaction phase the modes become mixed, exhibiting characteristics of both converging mode shapes simultaneously. This result has been validated experimentally by strain gages placed on the blade at mode specific locations. Kenyon concluded that fully determining how the exchange of mode shapes occurs during curve veering is essential in accurately predicting and measuring blade resonant response.

Another aspect studied to better predict blade vibratory response has been the effects of blade-to-blade variations that cause changing blade resonant frequencies known as mistuning. Large finite element models have been used in limited mistuning research, as the computations become too cumbersome with large model sizes. Cyclic symmetry can be used to reduce the finite element model size but using symmetry inherently makes blade variation around the rotor impossible since symmetry mirrors a single blade model around an axis to create the entire rotor. One attempt by Ottarsson et al. [1995] used variations in the calculations for a symmetric finite element model to effectively create a mistuning while keeping the model size much smaller and lessening the computational intensity.

Griffin [1988] experimentally researched mistuning for a low-speed bladed disk assembly through the use of strain gages. He defined the tuned-disk frequency as the frequency at which the entire bladed disk assembly would vibrate if all the blades were tuned. From his studies he found that the blades whose resonant frequency matched the tuned-disk frequency had the largest stress amplitudes.

Kenyon [1999] investigated blade response to inlet total pressure distortions on a blisk by measuring dynamic strain gage output coupled with a reduced-order analytical model to predict the blade resonant stress variations with respect to mistuning. He determined that blade structural mistuning and mechanical coupling had a relatively small effect in measured stress variations when compared to the effects of unsteady aerodynamic coupling. Experimental results were compared with results from the reduced-order model, and both agreed that unsteady aerodynamic coupling played a major role in the mistuned response of the blisk with a rough correlation of blade-to-blade stress amplitude variations.

2.3 Literature Review Conclusion

Over the course of gas turbine and compressor technology development a great deal of time and effort has been spent examining and understanding the effects of inlet distortion on a wide variety of operational parameters. The first area of concentration dealt with performance loss due to reduced stall margin and a loss in pressure rise. Many

experiments using many different techniques over the years have been tried to theorize, categorize, and summarize the cause and effect of varying total pressure inlet distortions with only an extremely small number of them discussed here.

In comparison to compressor performance studies, experiments and modeling of fluid-structure interaction and vibratory blade response are relatively new. The progress of computing power has led the way to make CFD and FEM viable options in place of extensive testing. While physical testing will likely never be eliminated from the design process, computer modeling will become more and more important and realizing the many ways to exploit the capabilities of the computer in distortion studies will be as important as the modeling itself. This research is an attempt to move distortion and vibratory blade response in a new direction by utilizing CFD results to excite blade response through the use of modal and harmonic analysis. While complete fluid-structure interaction codes exist, it is computationally expensive and possibly unneeded if it can be shown that results from manually adjoining CFD and FEM can produce promising results for "small" deflections as validated by experimental results.

With an ever-increasing push to cut cost while decreasing design, test, production and implementation time, it's likely inlet distortion studies on performance loss and structure life will never end. This research is just one attempt at reducing experimental testing time by using modal analysis to predict stress variation magnitudes induced from an aerodynamically forced vibratory response.

3 Experimental Data Conditioning and Collection

All data used during this research was provided by the USAF Compressor Research Facility (CRF) at Wright-Patterson Air Force Base in Dayton, Ohio. The data was acquired from tests that were run on a two-stage transonic, low aspect ratio compressor while operated at certain speeds and conditions known to produce rotor resonance. Many operating speeds were used to collect aerodynamic and aeromechanical data however only a small portion of the data collected will be the focus of this research, to be discussed later in greater detail. This chapter provides a partial summary of the "experimental procedure and data acquisition" of [Small, 2001] as an overview of the experimental facility, set up and procedure, and the characteristics of the data collected. Lastly, the reduction and manipulation of only the data related to the focus of this research will be discussed.

3.1 Experimental Facility

The CRF is comprised of three main buildings: the test building, the operations building and the electrical building. The test building houses the test chamber, flow conditioners, and the electric drive motors, while the electrical building houses the power supplies and transformers necessary to operate the drive motors. A schematic of the test section is shown in Figure 3-1. All experiment controls, data acquisition devices and test monitoring equipment are located in the operations building.

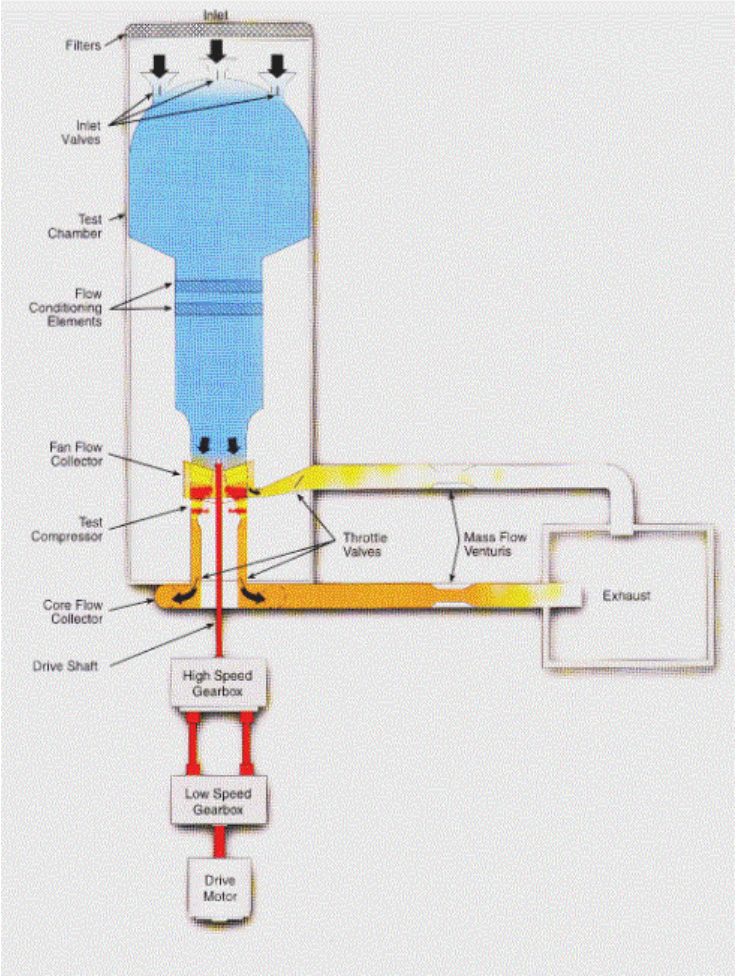

Figure 3-1: Test facility at the Compressor Research Facility, Wright-Patterson AFB [Morrow, 1993].

The test section uses the test compressor to draw atmospheric air through a number of devices used to regulate and control the airflow before entering the actual compressor bellmouth intake. Throttle valves are used to regulate the upstream pressure while flow conditioners are used to ensure the flow is straightened. The test chamber upstream of the compressor is 65 feet long and 20 feet in diameter. Once the air has passed through the test compressor it again passes through more valves to regulate downstream pressure, which ultimately controls the compressor pressure ratio. The flow is then discharged through a vertical flue back into the atmosphere. Venturis located just before the exit allows regulation of the mass flow through the test chamber and is capable of providing mass flow rates from 0-500lbm/s.

Two 30,000 horsepower electric motors and two gearboxes, one high and one low-speed, are available to choose from to control the test compressor speed. The speed is determined by the combination of the motor and gearbox selected for the test. The CRF uses a system called the Variable Speed Drive Control to set test speeds, control any changes in speed during a test, as well as provide safe automatic coast-down modes.

Data taken from the first stage in this two-stage compressor is the focus of this research. A picture of the first stage can be seen in Figure 3-2. The first stage is of modern design, called a rotor 'blisk' (contraction of blade and disk) and is made of a monolithic piece of titanium alloy. This means there is no dovetail joints present at the blade-disk interface therefore making the structure stronger by eliminating seems. This design feature should be noted, as it will become very important later.

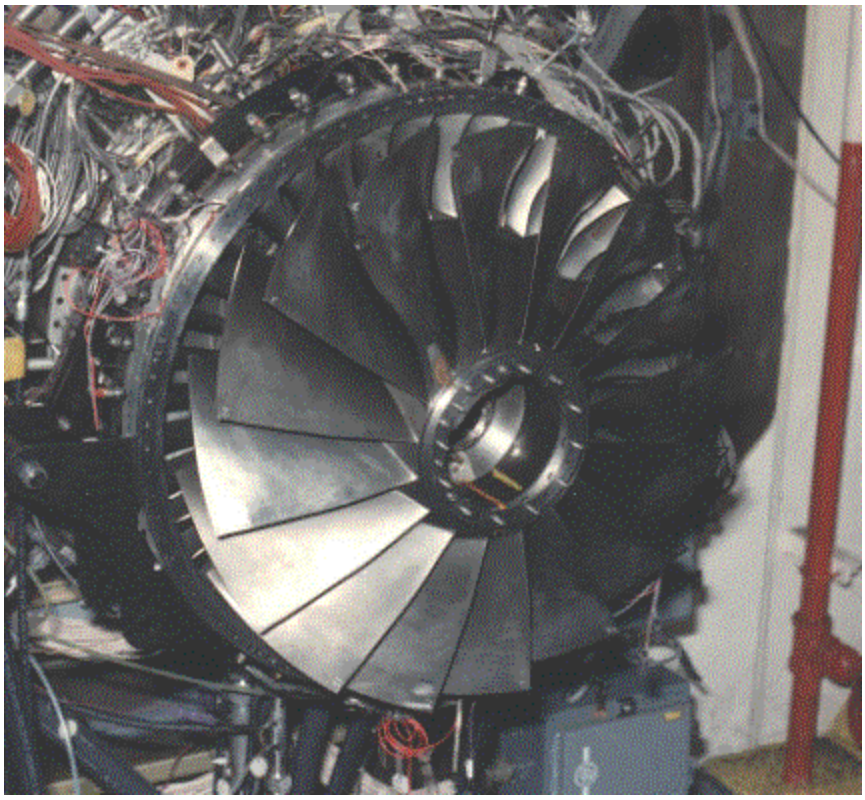

Figure 3-2: First stage blisk mounted on the test rig [Morrow, 1993].

Notice there are 16 low aspect ratio blades of modern design so the inlet conditions are temperatures near 300K and are supersonic about 45% span when operated at the operation design point. The second stage of the compressor is of traditional design with 40 blades mounted to the disk using the dovetail joints mentioned above; see Figure 3-3. Table 3-1 shows the geometric characteristics of only the first stage.

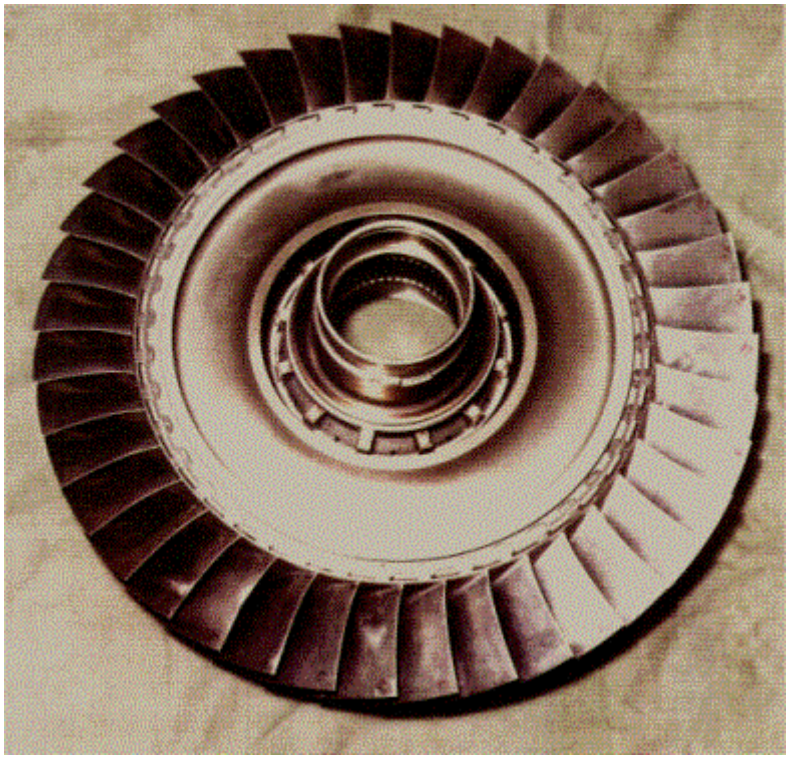

Figure 3-3: Second stage rotor [Morrow, 1993].

Table 3-1: First stage blisk geometry characteristics [Rabe et al, 1999].

Parameter	Value
Average Aspect Ratio	1.22
Rotor Tip Radius (in.)	13.87
Inlet Radius Ratio	0.33
Average Radius Ratio	0.47
Average Tip Solidity	1.50
Maximum Thickness/Chord	0.028

3.2 Experimental Procedure

To collect data on aerodynamic and aeromechanical effects of pressure distortion, devices capable of generating distortions in the airflow are needed. Distortion screens, as discussed earlier, were used for this purpose and were located downstream of the bellmouth but approximately 1.5 engine diameters in front of the leading edge of the first stage rotor. To measure the pressure distortions caused by the screens, pressure probes were inserted at five radial immersions. The location of the probes was determined by dividing the frontal area of the compressor into five equal annuli with respect to mass flow [SAE, 1999]. Each probe was positioned in the center of its annulus at approximately ½ diameter in front of the first stage rotor. A total of eight groups of probes, called rakes, were positioned around the circumference of the compressor equally spaced apart. The radial position of each probe within a rake is shown in Table 3-2 as measured from the outside diameter inward. A cross section of the experimental setup is shown in Figure 3-4. Total pressure was also measured between each stage by stator vane-mounted probes imbedded at three locations equally spaced around the circumference; however this data is not relevant to the focus of this research and is therefore not included.

Table 3-2: Radial locations of the inlet total pressure probes [Morrow, 1993].

Immersion	Radial Distance from O.D. (in).
1	0.74
2	2.31
3	4.11
4	6.33
5	9.57

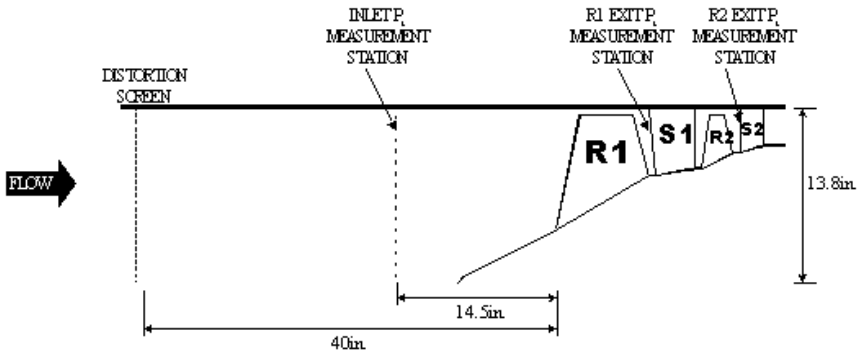

Figure 3-4: Cross section of the experimental setup [Morrow, 1993].

A distortion screen used to create total pressure distortions, as mentioned earlier, is shown in Figure 3-5. The screen is constructed of several sections of wire mesh with varying porosity. The idea behind the screen was to gradually vary the distortion level while moving in the circumferential direction and therefore create a smooth, steady state, sinusoidal pressure distortion. The screens succeed in causing total pressure distortions by reducing the axial momentum of the air as it passes through the screen and therefore reducing the dynamic pressure, a component of total pressure, as seen by the rotor blades. During testing two screens were used, a 3 per rev and an 8 per rev screen. Figure 3-5 is that of a 3 per rev distortion screen.

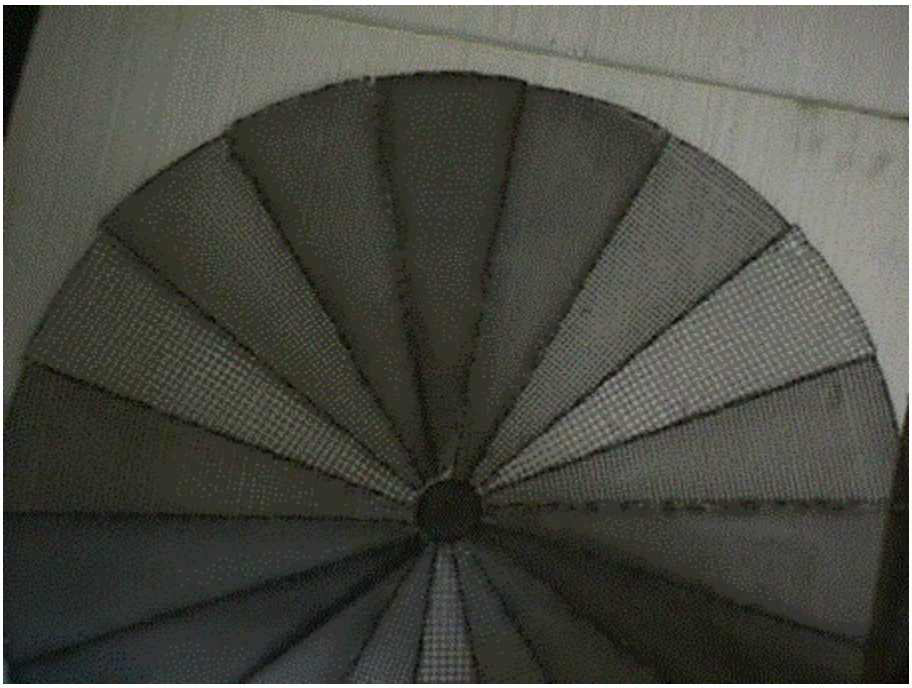

Figure 3-5: An example of a 3-per-rev distortion screen [Morrow, 1993].

To obtain a high resolution of circumferential pressure data while keeping the number of probes needed reasonable, the screens were rotated. Each distortion screen was mounted on a screen rotator comprised of support struts to which the distortion screens were attached and an external drive motor. The motor is located outside the flow field to prevent unwanted airflow blockage. If the screens had not been rotated, it would have been essential to mount a pressure probe at every location data was desired. This scenario, while possible, is certainly not desirable due to the sheer number of probes required as well as the increased flow blockage caused by the extra probes.

Using the rotating screen method, a single probe's data could contain a full 360 degree sweep of the pressure distortion. To resolve the data spatially the position of the screen must be related to the time at which the sample was taken. A sample rate high enough with respect to the rotation speed of the screen is required to ensure the high spatial resolution desired. However, it must be recognized that the distortion screens are designed to create steady state pressure distortions and therefore the speed at which they are rotated must be considered. If the screens are rotated too quickly, a rotational component is added to the distortion that is undesirable regardless of increasing the

sampling rate. A study by Williams [1999] determined that a rotation speed of 2 degrees per second is sufficiently slow enough to consider the distorted flow quasi-steady.

3.3 Data Characteristics

The total data set consists of circumferential total pressure measurements collected for 11 different operating points of the test compressor. The 11 operating points are comprised of 4 different mass flow settings at 3 different rotational speeds. The four mass flow settings are as follows: Normal Operating Line (NOL), Near Stall (NS), Peak Efficiency (PE), and Wide-Open Discharge (WOD). The three test speeds are 9100 rpm, 9500 rpm, and 13200 rpm which corresponds to 68.5%, 71.5%, and 99.3% respectively, of design speed. (Note: There are only 11 operating points instead of 12 because NS and PE are coincident at 13200rpm).

As mentioned earlier, two distortion screens were used during testing, a 3-per-rev and an 8-per-rev, however both screens were not used for all operating points. The 3-per-rev screen was used at 9100 rpm only while the 8-per-rev screen was used at 9500 rpm and 13200 rpm. As noted before, only a small portion of the data was used for this research focus, that being the 3-per-rev distortion screen operated at 9100 rpm and WOD only. In addition, this data was filtered to a pure 3-per-rev signal that will be discussed in greater detail in the next section.

3.4 Raw Data Reduction and Manipulation

A pure 3-per-rev distortion pattern is almost impossible to create in the test chamber due to all the mounting hardware and probes. The seams where the various wire mesh pieces are joined together on the distortion screen along with the struts to which the distortion screen is attached and the pressure probes and rakes all add unwanted distortions to the flow. For this research focus it is desired to have the purest 3-per-rev pressure distortion possible to isolate the blade response as a result of only the given pressure distortion. Gary Ostdiek at CRF used a curve fit of the data to remove unwanted distortion. The

data were taken at 5 different radii and with a point taken about every half degree. The data were then arranged in a spreadsheet with the curve fit divided into 50 radii by 448 circumferential points in an array. Figures 3-6 and 3-7 show the pressure profile before and after the unwanted distortion was removed from the original 3 per rev data, respectively. A sample from Immersion 3 (mid-span) shows the total pressure with unwanted frequency content in Figure 3-6 and again in Figure 3-7 with the unwanted frequency content removed. The numbers on the right side of the legend indicate total pressure in psi in both figures.

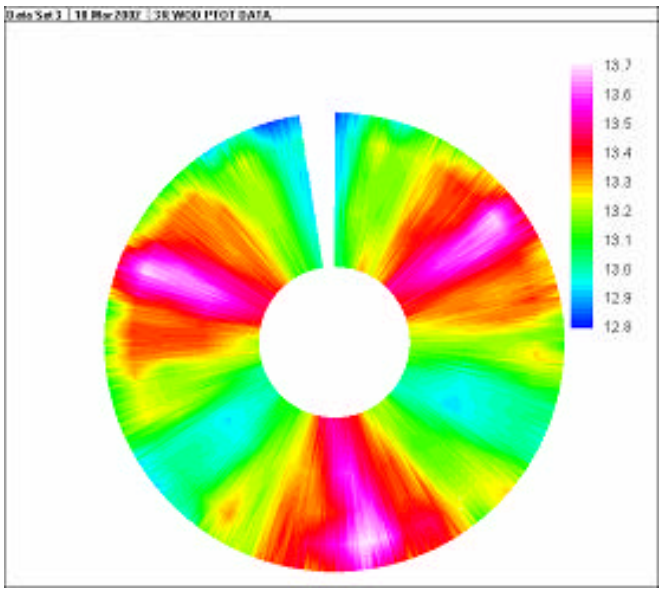

Experimental Total Pressure at Immersion 3 (mid-span)

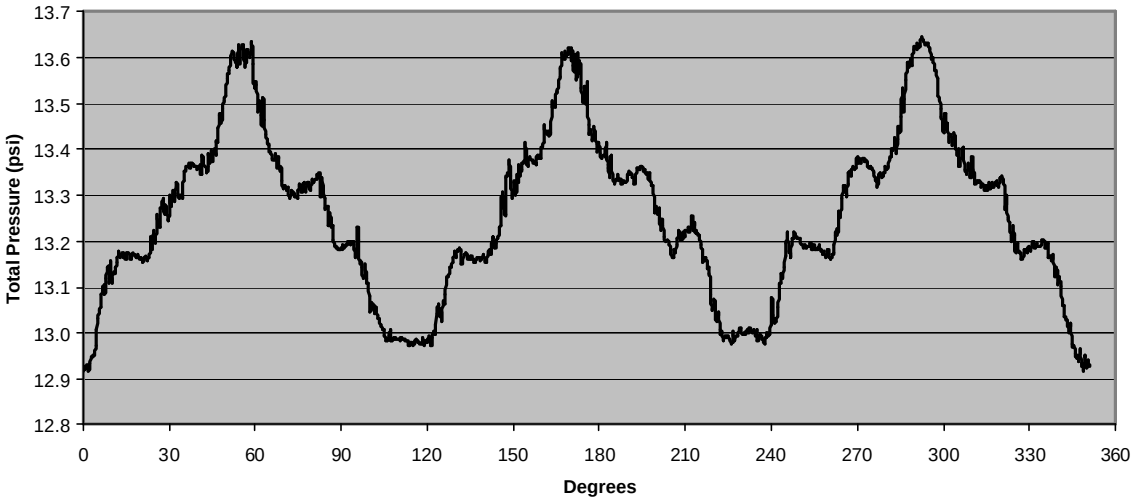

Figure 3-6: Experimental 3-per-rev total pressure distortion.

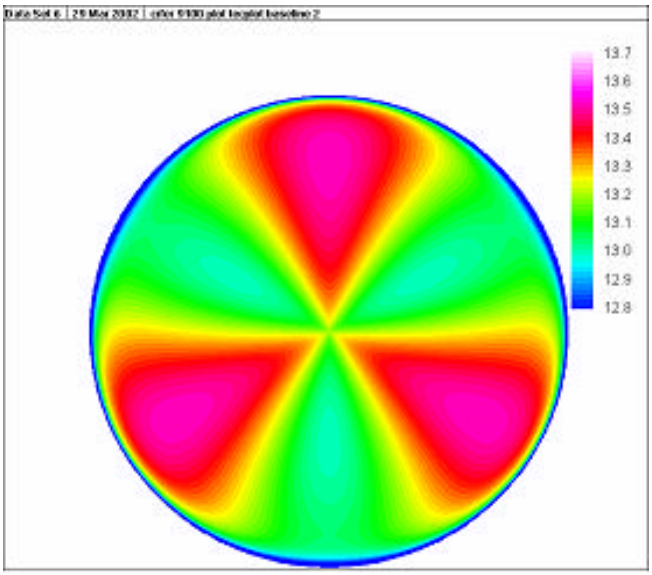

Model Total Pressure at Immersion 3 (mid-span)

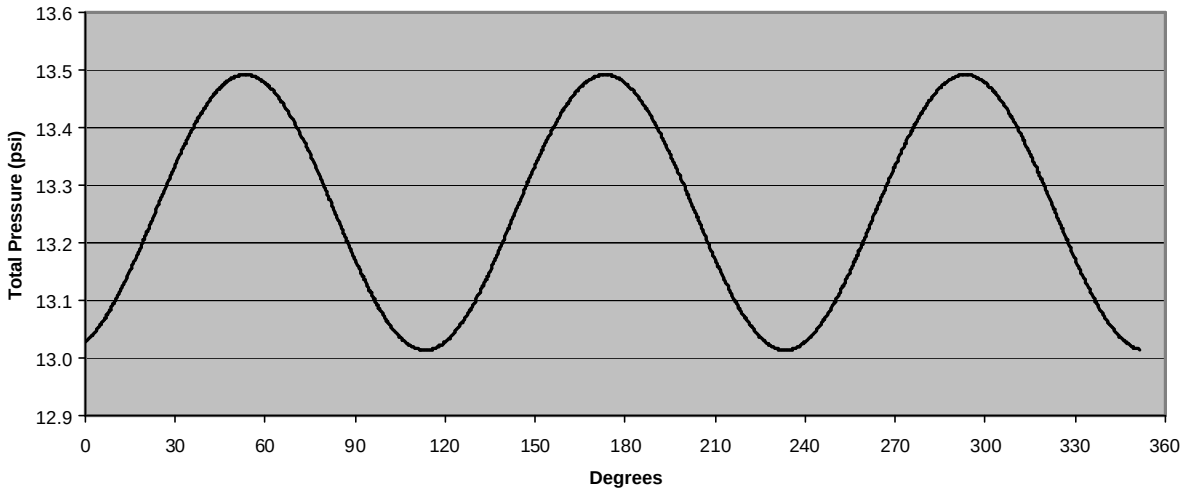

Figure 3-7: Total pressure 3-per-rev model.

After the pressure profile was modified it was then sent to Dr. Hah at the NASA-Glenn Research Center for further development. Dr. Hah used the pressure profile as the inlet conditions for a single blade passage CFD model of the first rotor stage. From this model he was able to create a blade surface pressure profile for both the pressure and suction sides of the blade. Since the inlet distortion is assumed steady state and each sinusoid was identical to the other two in the 3-per-rev distortion, only 1/3 of the

distortion profile was needed as the results could be duplicated around the remaining 2/3 of the circumference.

A 64 by 29 element grid in the streamwise and spanwise direction, respectively, was used to describe the blade surface on both sides and data was collected for 3 different cases. The 3 cases consisted of a 3-per-rev distortion with 80%, 100%, and 120% of the original pressure distortion magnitude. Before running each case through the CFD code the level of distortion was simply multiplied by either 0.8 or 1.2 to change only the magnitude but not the pattern. It is important to understand that the three cases are not independent experimental results from changing the actual distortion screen porosity or any other parameter. Only one case was actually tested experimentally, the 100% case; all other cases are just an amplification or attenuation of the resulting distortion level measured experimentally for the 100% case. However, due to the possible non-linearity of the calculated blade surface pressures, it can not be assumed that the blade surface pressure profile generated will simply be a constant multiple across the entire face equal to that of the inlet pressure profile. For example, the blade surface pressure profile for the 80% case cannot be assumed to be 80% of the value found for the 100% case at any grid point on the blade

I was supplied six data files from Dr. Hah at this point, one for each distortion level on each side of the blade as well as the CFD grid point locations. Upon receiving the data, some reformatting and manipulation was required due to varying reference methods used to describe the data. Multiple coordinate systems were used and nodal numbering schemes had to be resolved to one single system so that data could be applied to the FE model created using the grid points supplied.

4 Finite Element Model Development

A finite element (FE) model was developed for the first stage rotor blade using the CFD grid points as the nodal coordinates in the model. Before this method of describing the geometry was chosen, other methods were considered and attempted in order to weigh the pros and cons associated with each. In an ideal situation, a parametric model describing the exact blade geometry would have been desired, however at the date this blade was designed such models were not prevalent and therefore one was not made. In fact, no data containing the exact blade geometry could be located for this research, leaving only pre-existing finite element models to be used. At some point a NASTRAN model was developed for vibrations analysis but the mesh density was very coarse and did not match the grid points used for CFD and therefore was not used.

4.1 Choosing the Correct Modeling Method

In preliminary model development and testing a solid model was created by using a limited number of points measured from a scale drawing and interpolating the curved surfaces between them. This method proved to be accurate to solve for the natural frequencies of the blade as compared with frequencies measured experimentally. However, natural frequency is largely dependent on material properties and the general geometry of the object being tested for low order modes like the ones here, with slight changes in the geometry affecting the solution very little, and is therefore not a conclusive way to test whether the interpolated blade curvatures were those of the actual blade.

A second attempt to create a solid model was executed using a slightly different method. An approximate solid model could be developed by importing the CFD grid points into ANSYS® and using them to more accurately describe the blade geometry. Many attempts were made to create splines through the many points in the streamwise direction. Splines were also used to create the leading and trailing edge of the blade.

Using the splines as borders, many areas were created to describe the surfaces in small strips. By selecting and adding the relevant areas, a volume can be created (picture selecting the sides of a cube as areas that describe the boundaries of the volume created by them). Adding all of the volumes together creates a single volume and a solid model that describes the entire blade is created. However, remember that the initial step employed the grid points to define the geometry, and as a result the curvature of the blade is still approximated, albeit much better, but not exact nonetheless. Splines do not always follow the path desired and areas are not easily created on curved surfaces unless a process called 'skinning' is used. Even then the area created does not always adjoin the splines picked as the borders used to describe the area. Therefore, when attempting to create a volume from areas with discontinuities between them, obvious problems arise. In the end, the attempt to create a solid model in this fashion was abandoned due to numerous problems that prevented a continuous solid from ever being created.

The advantage of starting the analysis with a solid model allows the user to define and refine the mesh type and density applied to the model during analysis. Refining a mesh in FE analysis becomes very important as it allows the convergence of a solution by continually making the mesh more refined until the value in question no longer changes, in this case the natural frequency. However, since the true natural frequency of the blade was already known from experimental tests, this allowed one more and final option for developing a model.

The third model again used the CFD grid points as nodal locations in 3D space to describe the blade geometry. Instead of attempting to back out an accurate solid model, the nodes created were simply connected to create elements directly. At this point a rectangular element was chosen and a small code was written to read in the node locations of each of the nodes defining the 8 corners of the cube, create the element and then proceed to the next node. After this was finished, a complete FE model was created with a fixed mesh density. In order for this model to be used, the natural frequency solution as found by ANSYS would have to be close to the actual natural frequency with the given mesh density since no refinement was possible without additional extensive work to subdivide the elements. To accurately model bending with the element type used, ANSYS suggests at least a thickness of three elements in the primary direction of

bending. Since CFD only needs surface nodes to evaluate the flow around the blade, two rows of internal nodes had to be created using TECPLOT® to interpolate between the two surfaces. Initially only 3 rows of elements were created and the model was tested. The natural frequency found was within 2.3% of the experimental value and therefore the model was considered valid. It should be pointed out that the blade surfaces have been discretized by the flat element surfaces but this is of no consequence in the vibration analysis since the natural frequencies were found to agree. This may not be the case if the model were used for other types of analysis. The final FE model used for this analysis is shown in Figure 4-1. A black dot has been placed at the leading edge tip in both views as a point of reference.

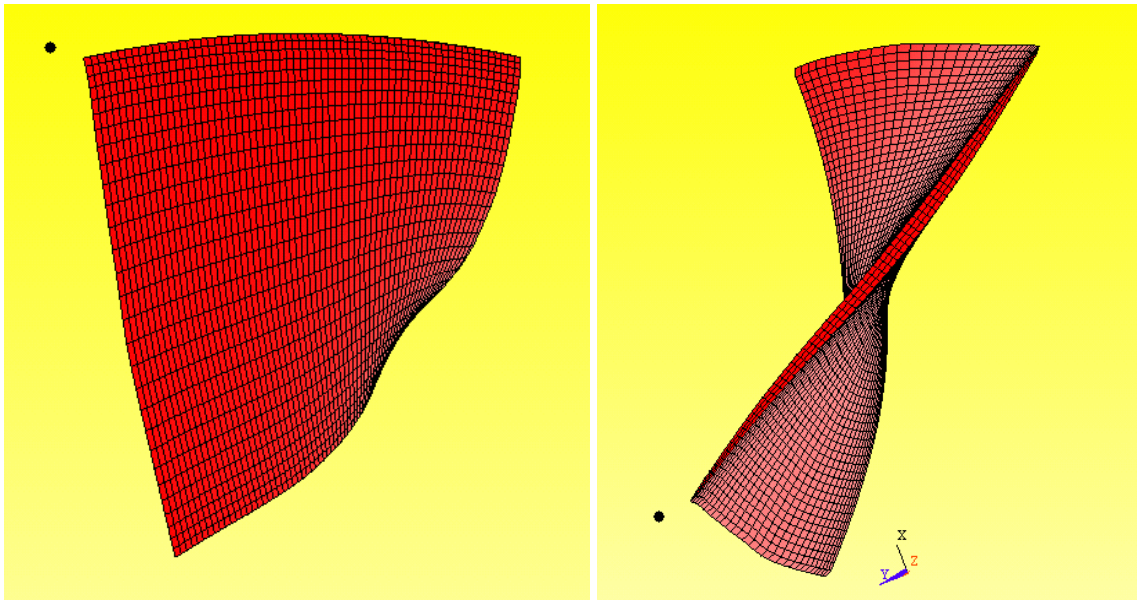

Figure 4-1: The 5568-element model used for analysis.

4.2 Model Properties and Constraints

As mentioned previously, the blades are not connected to the hub with a dovetail configuration on the first rotor stage. Thus, there is virtually no damping provided by the 'hub', which allows for it to be eliminated from the model and the blade to be assumed constrained as a cantilevered beam. In theory, all 16 blades are identical and therefore

should posses the same natural frequency. In reality, however, this is not the case due to mistuning. For this research it is assumed that all the blades are identical. Therefore for it is assumed that response is equal allowing only one blade analysis to speak for the group. The material properties used in the FE model are detailed in Table 4-1.

Table 4-1: First stage rotor FE model material properties.

	Titanium Alloy (Ti-6-4)	**Pure Titanium (Ti)**	**Percent Difference**
Density (?)	0.161 lbm/in^3	0.175 lbm/in^3	+8.2 %
Modulus of Elasticity (E)	16.5x10^6 psi	14.8x10^6 psi	- 10.3 %

The exact material properties were still unknown to the author at the time model creation started and therefore the values for pure titanium were used, as opposed to the titanium alloy actually present. The difference in material density and modulus of elasticity is also shown in Table 4-1. The pure titanium material properties were used throughout the entire analysis since the model validation phase, which included original MATLAB® code to verify the numbers ANSYS calculated on a much simpler two-element beam, used pure titanium. To change the material properties midway through the analysis would have required resolving all the initial steps leading up to the present calculation. Furthermore, the non-exact material property values gave extremely good natural frequency results. The process was repeated once the material used, titanium alloy Ti-6-4, became known. An unintentional positive outcome of this result is that it is shown that a small amount of approximation in material properties can be used without adversely affecting the solution's accuracy.

4.3 Rotational Effects

To accurately model the state of the rotor blade during operation, the blade must be rotated around a point equal to the distance of the engine's center of rotation at the

correct speed. The model was therefore set to simulate 9100rpm throughout the analysis. Spinning an object can have two main effects: the object becomes artificially stiffened in certain directions due to the centrifugal forces pulling on the mass; and, the object's shape will change if portions of the mass are not aligned along a line drawn between the center of rotation and the object's center of mass. The rotor blade is subjected to both of these effects, which introduces another difficulty in modeling not yet discussed.

Compressor blade designers design the blade shape for the intended operation point keeping in mind the blade shape changes as a result of centrifugal forces. The shape of the blade at the design operation point is known as the "hot geometry," while the shape of the blade sitting stationary is known as the "cold geometry." The cold geometry must be determined in a way so that the blade will assume the intended geometry at the design point. This change in blade geometry is known as "untwist." The blade will continue to untwist as the speed at which the engine is operated increases.

For CFD analysis the hot geometry is all that is needed since the blade shape alone determines how the fluid flows around it. This presents a potential problem in using the CFD grid points to define the blade used in vibration analysis. While the natural frequencies were used to compare and validate the model, the mode shape is the end result desired. The natural frequency only indicates the point within the frequency spectrum that excites the object, however it says nothing about how the object moves once excited. The mode shape contains information on how the object moves, giving the direction and relative magnitude of any given point in relation to any other point within the object. All magnitudes are relative, as no absolute magnitude of deflection is known until the magnitude of the force exciting the object is defined. It now becomes apparent that if the shape of the blade before excited is different at different states ("hot" versus "cold") then it is possible the mode shapes will differ greatly for the same mode on two related, but different blade shapes.

The problem arises when considering the centrifugal stiffening and untwisting of the blade simultaneously. Using the hot geometry grid points from the CFD calculations gives the correct blade shape without using centrifugal force induced untwist. This alone would not be an issue if the centrifugal stiffening were not a concern. However, it is, and so this does become a concern. Ideally, the cold geometry would be desired so it could

be spun at the correct operational speed and therefore introduce the artificial stiffening and untwist simultaneously as it occurs in reality. Again, due to the age of the design, computer models were not available that describe the cold geometry. Only later were hot geometry models generated for CFD calculations, and therefore a way to handle the obstacles had to be determined.

Since the natural frequency increases with increasing stiffness, the rotational speed directly determines the amount of stiffening that occurs and consequently the natural frequency. Knowing that all the data being considered was taken at 9100rpm means a possible solution was to increase the stiffness in the material property definition until the hot geometry had the correct natural frequency while sitting stationary. The amount to increase the stiffness would have to be determined by a trial and error approach and it was decided to explore other options before attempting this solution.

I decided to calculate and compare the mode shapes for the hot geometry stationary with the hot geometry spun at 9100rpm. While it is true that the hot geometry spun at 9100 rpm gives an incorrect blade shape, the degree of untwist should be approximately equal to that the blade undergoes while untwisting from the cold to the hot geometry. If the difference in mode shape turned out to be minimal between the hot geometry spun and unspun, then it could be argued the difference would be very similar between the cold and hot geometry. In addition, ANSYS is a linear finite element code, which means small deflection theory must be assumed. This means that the blade deflection due to untwist must already be assumed to be very small. If this assumption were not found to be correct, then the entire blade model would be invalid as ANSYS would be incapable of accurately calculating a solution, as the blade would untwist too much for a linear code solution. However, the test showed a maximum difference in mode shapes of less than 1% using a root-mean-square calculation to sum the differences between each node of the model. Therefore it was decided that mode shapes from the hot geometry spun at 9100 rpm could be used. This means that while the blade shape would be slightly incorrect, the natural frequency and the mode shape will be approximately correct as the centrifugal stiffening and untwist plays a very small role in changing the mode shapes for the case being considered.

4.4 Finite Element Model Summary

The finite element model used for all analysis was constructed from the CFD grid points that described the hot geometry. This geometry was constrained only along the base of the model for zero displacement and rotation in all directions where it attaches to the "hub", and was spun at 9100 rpm. It consisted of 5568 Solid 45 "brick" elements with a 3-element thickness in the direction of primary bending. The material properties used were those of pure titanium and titanium alloy Ti-6-4 as given in Table 4-1 with a damping ratio of 0.0083 as determined by CFD calculations [Breard, 2002].

5 Analysis and Results

The main research goal of developing a model representing the blade and how it responds to total pressure distortion and therefore saving much time and money by partially eliminating such extensive testing is the driving factor for determining the analysis methods. Remember the three main goals: (1) create an accurate finite element (FE) model of the ADLARF fan blade for eigenvector extraction; (2) identify dominant engine order modal force magnitudes based on coupling computational fluid dynamics (CFD) generated total pressure distortion and FE generated eigenvectors; and (3) determine the relationship between the magnitude of the modal force and the total pressure distortion level used to drive the system. The modal force represents the generalized force used to drive the FE model of the ADLARF fan blade at a given mode. Goal (1) was addressed in the previous chapter under Finite Element Model Development. The remaining goals will be addressed now.

5.1 Finite Element Generated Eigenvectors

The first step in determining and analyzing the reaction of the blade is to identify the way in which it naturally deflects under free vibration. Free vibration occurs when an object is given an impulse to excite the system but not continuously applied in any constant or changing rate. Experimentally, free vibration is often tested by suspending the object from a string or bungee chord, then striking it with a hammer and measuring the response with an accelerometer or a laser vibrometer. In the case of the compressor blade, one side is attached to the "hub" and is constrained from motion in all directions and therefore a shaker rig could be employed to test free vibration under these constraints. A shaker rig allows the object to be securely fixed to a moving platform that undergoes a frequency sweep, record the response over the range tested and determine the natural frequency, or eigenvalue, of the object by referencing the frequency at which the largest deflections occurred.

However, determining the mode shape, or eigenvector, experimentally is much more difficult. To accurately describe the eigenvector one needs to know the magnitude and direction that each "point" on the object moves. The word point is used in quotations to underline the fact that no discrete points exist on an object. Therefore, experimentally testing for eigenvectors would require numerous accelerometers, which would ultimately change the system with their added mass, or a scanning laser vibrometer that is capable of quickly scanning the entire surface of the blade as it deflects while being excited at any given frequency. Again, in the case of the compressor blade, the rotating nature of its operation introduces difficulty in experimental tests. Ways to use a scanning laser vibrometer in such an environment have been researched, but are not presently being used at CRF for this purpose. This is where the advantages of a finite element model can be realized.

In a FE model, mass and stiffness matrices are constructed and the equations of motion and therefore the eigenvectors can be solved for directly. The motion of the "points" on the object mentioned previously become the nodes present in the model. These nodes also represent the mass in the system. A finite element model divides the entire mass of each element and distributes it to the nodes at the corners. In this case, the solid 45 brick element is a rectangular shape and therefore has 8 nodes that make up the 8 corners of the brick. Therefore the mass of any given brick element is divided by 8 and assigned to each of its nodes. Most nodes (except those on the exterior blade corners) are connected to multiple brick elements and therefore receive an additional contribution to their mass as well.

Simplifying the situation for the sake of explanation, each node can be thought of as a single degree of freedom system consisting of a mass, spring, and damper and only allowed to deflect in one direction. The familiar diagram associated with this system is shown in Figure 5-1. The entire blade, however, is comprised of many nodes and must be evaluated as a multiple degree of freedom system where the motion of each mass affects all others in the system. A diagram showing a simple multiple degree of freedom system is given in Figure 5-2. In reality even one node on the blade contains more than one degree of freedom as it is allowed to deflect in all three directions, X, Y, and Z.

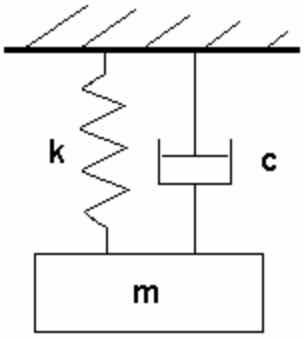

Figure 5-1: Single degree of freedom model.

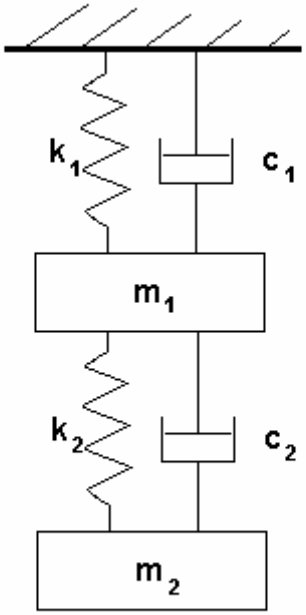

Figure 5-2: Multiple degree of freedom model.

The equation of motion for a single degree of freedom model is given by

$$m\ddot{x} + c\dot{x} + kx = F(t)$$

Equation 5-1

where m, c, k represent the mass, damping, and stiffness of the system, respectively. Realizing that the natural frequency, $?_n$, is equal to the square root of the stiffness divided by the mass and introducing ? as the damping ratio then the equation can be rewritten as

$$\ddot{x} + 2z w_n \dot{x} + w_n^2 x = F(t)$$

Equation 5-2

For modal analysis the same equations of motion apply and for multiple degrees of freedom they take on a matrix form. The nomenclature for the force acting on the system has been changed to represent a periodically changing force representative of the total pressure inlet distortion. In addition, most damped systems are analyzed in modal analysis as undamped. Damping is applied after the solution to find the natural frequency and therefore the damping has been removed from Equation 5-3.

$$M\ddot{x} + Kx = f\ e^{iwt}$$

Equation 5-3

The variables for the mass and stiffness become capital M and K to denote they are of matrix form. Here x is a vector containing all the modes of the system.

$$x = \sum_j ?_j(t)\tilde{F}_j$$

Equation 5-4

Substituting and premultiplying by $\tilde{F}_i^T$ gives

$$\sum_j \ddot{h}_j(t)\Phi_i^T M\Phi_j + \sum_j h_j(t)\Phi_i^T K\Phi_j = \Phi_i^T f\, e^{iwt}$$

Equation 5-5

Where

$$\Phi_i^T M\Phi_j = \begin{cases} 0 \to i \neq j \\ 1 \to i = j \end{cases} \quad \text{and} \quad \Phi_i^T K\Phi_j = \begin{cases} 0 \to i \neq j \\ w_i^2 \to i = j \end{cases}$$

Equation 5-6

Which then reduces to

$$\ddot{h}_j + w_i^2 h_j = \Phi_i^T f\, e^{iwt}$$

Equation 5-7

Finally, solving in matrix form for the generalized force becomes

$$[I]\{\ddot{?}_i\} + \begin{bmatrix} w_i^2 & & \\ & \ddots & \\ & & \end{bmatrix}\{?\} = \{F_i^T f\} e^{iwt}$$

Equation 5-8

So that the total modal force, F_j, is the projection of the force on the mode shape.

$$F_j = \Phi_i^T f$$

Equation 5-9

Using ANSYS to solve the equations of motion for the finite element model allow the first three modes shapes to be solved and the resulting eigenvectors to be output to a file. Now each node on the model has a direction and relative magnitude associated with it for each mode. The first three modes solved for are 1st flexural, 2nd flexural, and 1st torsional and were mass normalized. A table showing the error associated with each

mode from testing the hot geometry spun and unspun was constructed as shown in Table 5-1.

Table 5-1: Eigenvector RMS error calculation results.

Mode	Average RMS Error (%)
1	0.238
2	0.356
3	0.929

A Campbell Diagram is often constructed and implemented to identify problem areas of engine operation. One is presented in Figure 5-3. The diagram is constructed by testing the blade, either experimentally or using FEM, to determine the natural frequency over the entire range of operation by evaluating the system at incremental steps and plotting those points at their respective speed of rotation. Connect the points and the three solid lines are created, each showing how the natural frequency increases for each mode. Next, the "per-rev" lines are added, in this case from one to eight. A per-rev line indicates how many excitations a blade will encounter by traveling one circumferential distance. Knowing the data being analyzed was taken at 9100rpm with a 3-per-rev distortion screen used, we can see a problem area is likely to exist because this 3-per-rev source of excitement occurs at 435 Hz while operated at 8700rpm which coincides with the first natural frequency associated with the 1^{st} flexural mode. This area is highlighted by a red circle on the diagram. In fact, a Campbell Diagram similar to this one was constructed before the experimental testing took place to target problem areas as operation at these points is extremely dangerous and destructive. As a result, the data was taken at 9100rpm where the excitation occurs at 455 Hz and therefore still excites the first mode greatly, but not enough to induce deflections large enough to be destructive. The first mode shape is therefore of greatest concern with the largest deflection and modal force expected. From Table 5-1 it is reassuring to see the first mode has the least amount of error, as it will be the most important.

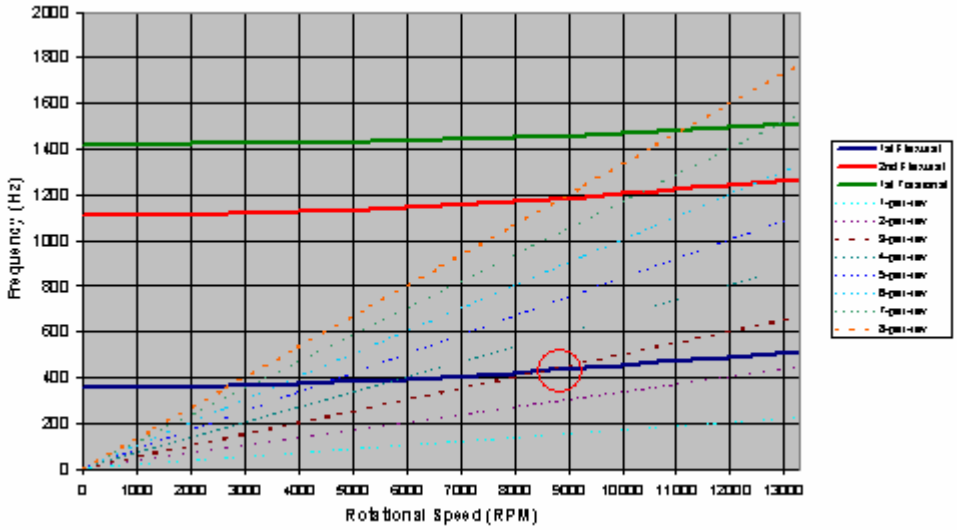

Figure 5-3: ADLARF 1st stage compressor Campbell diagram.

5.2 Generalized Forcing Function

Using modal analysis to determine the generalized forcing function, it is required to know how much of the pressure on the blade surface contributes to moving the blade in the same direction as the mode shape. The total pressure data as received from Dr. Hah only consisted of total pressure magnitudes at the given time steps. However, pressure can only act normal to a surface, so normal vectors had to be determined along both blade faces at each nodal location. Tecplot was used for this step and the normal vectors were associated with the pressure magnitudes using nodal coordinates. Normal vectors for the leading and trailing edge of the blade were eliminated since determining a normal for an edge is an ill-posed problem and as a result the eigenvector data from all nodes along the leading and trailing edge were not used.

Now that the mode shape and total pressure directions were known in 3-dimensional space acting through each of the nodes on the blade, a projection of the force due to pressure in the direction of the eigenvector could be determined. This requires an inner product to be taken. An inner product consists of multiplying each x, y, z

component of the pressure with the matching component in the eigenvector and then summing the results from each component.

$$\sum (E_i P_i + E_j P_j + E_k P_k) = \frac{1}{\sqrt{m}} * P$$

Equation 5-10

After each component has been summed for every node, the resulting values are summed together on both blade surfaces for the solution. Finally, to acquire a force instead of a pressure, the elemental area of the pressure and suction side were averaged and multiplied through as shown below.

$$GFF = \frac{1}{\sqrt{m}} * PA = \frac{1}{\sqrt{m}} * F$$

Equation 5-11

The solution is a single value indicating the relative magnitude of the generalized force on the blade for the time step evaluated. To show how this changes with time, the inner product is repeated and plotted for each time step. As mentioned previously, only 1/3 of the distortion pattern was used in the CFD calculations so the generalized forcing function results were conditioned to represent a full annulus. This included copying the results twice and adding them tip to tail effectively expanding the results around the full annulus. Second, to give a spatial representation, the time steps were converted to an angular position from 0 to 360 degrees. Lastly, the time steps were arbitrarily assigned during the CFD calculations so conversion to angular positions did not result in all the peaks of the sinusoidal pressure distortion being aligned, therefore the data from different simulations were phase locked for a more physical representation and to make result comparisons easier The inner product and results conditioning were done with Excel and the results are shown below in Figure 5-4 through Figure 5-9.

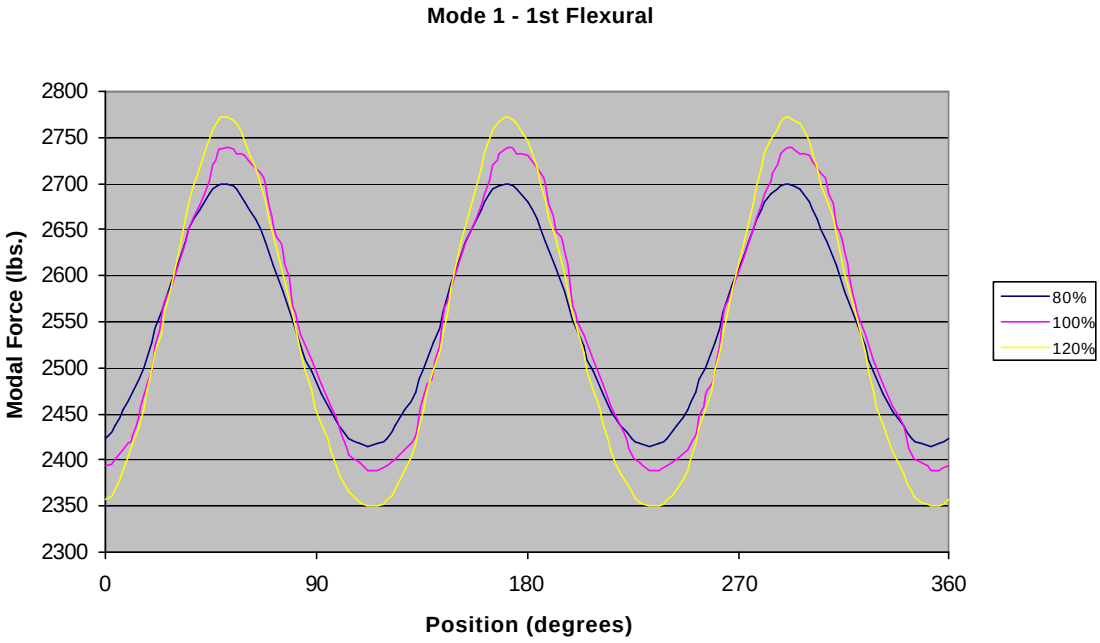

Figure 5-4: 1st Mode - Modal force as a function of distortion level.

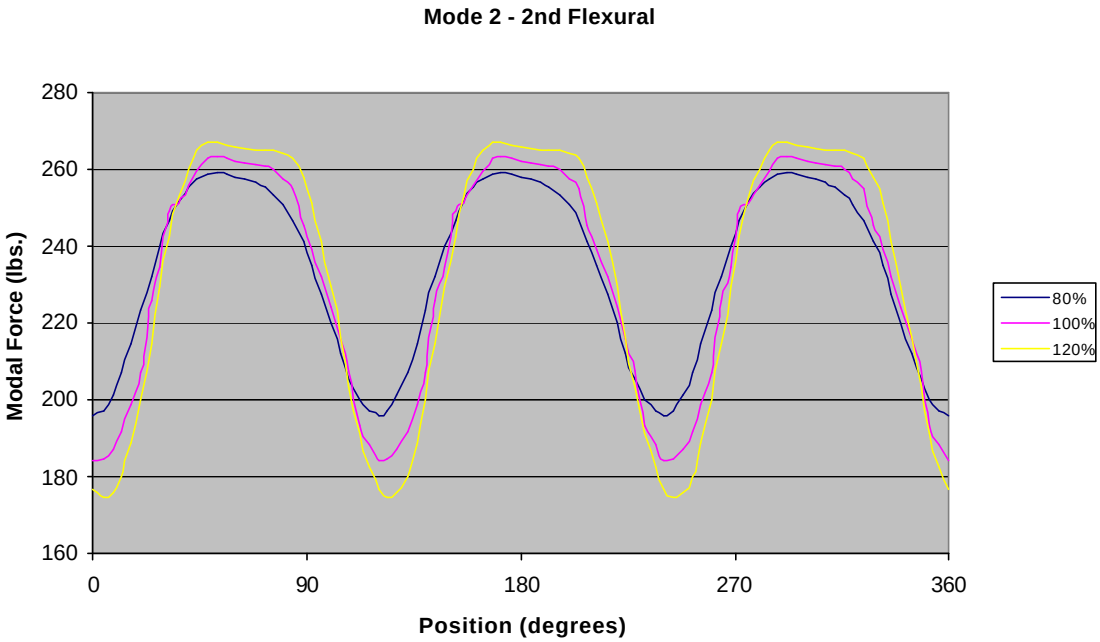

Figure 5-5: 2nd Mode - Modal force as a function of distortion level.

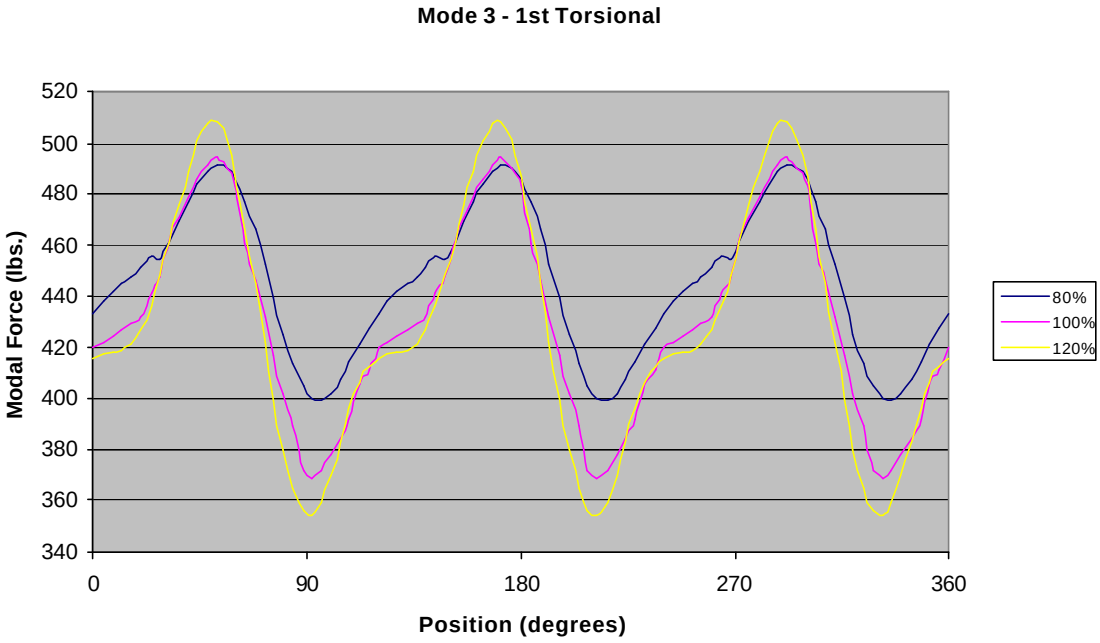

Figure 5-6: 3rd Mode - Modal force as a function of distortion level.

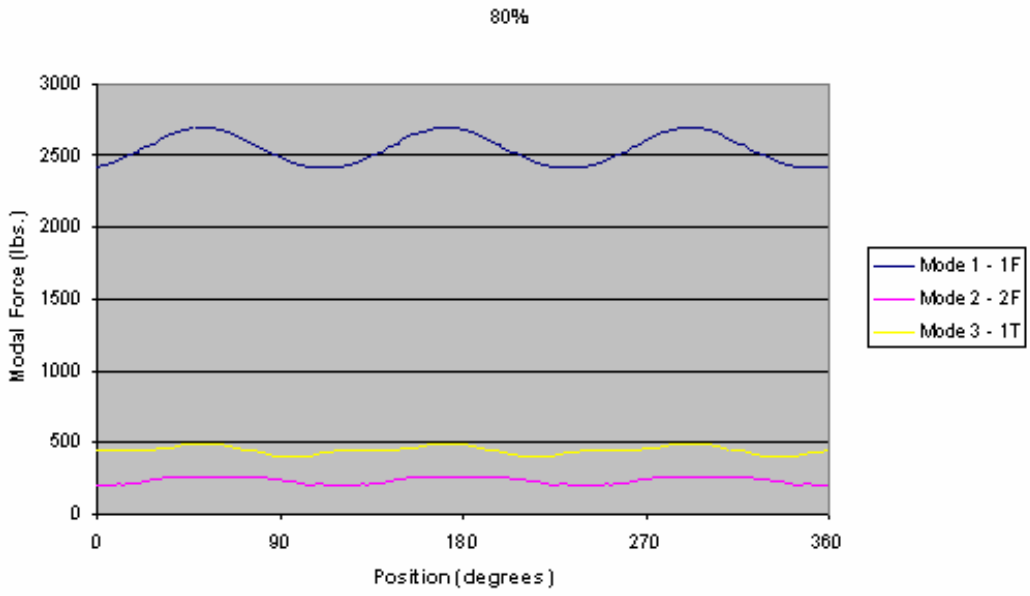

Figure 5-7: Modal force comparison at the 80% distortion level.

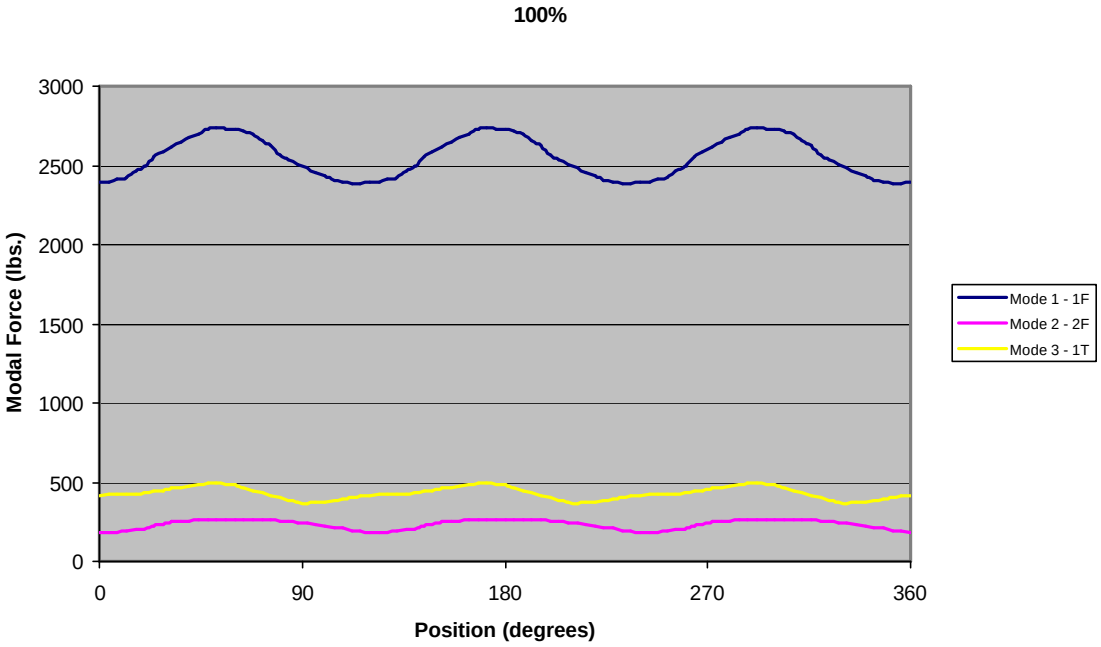

Figure 5-8: Modal force comparison at the 100% distortion level.

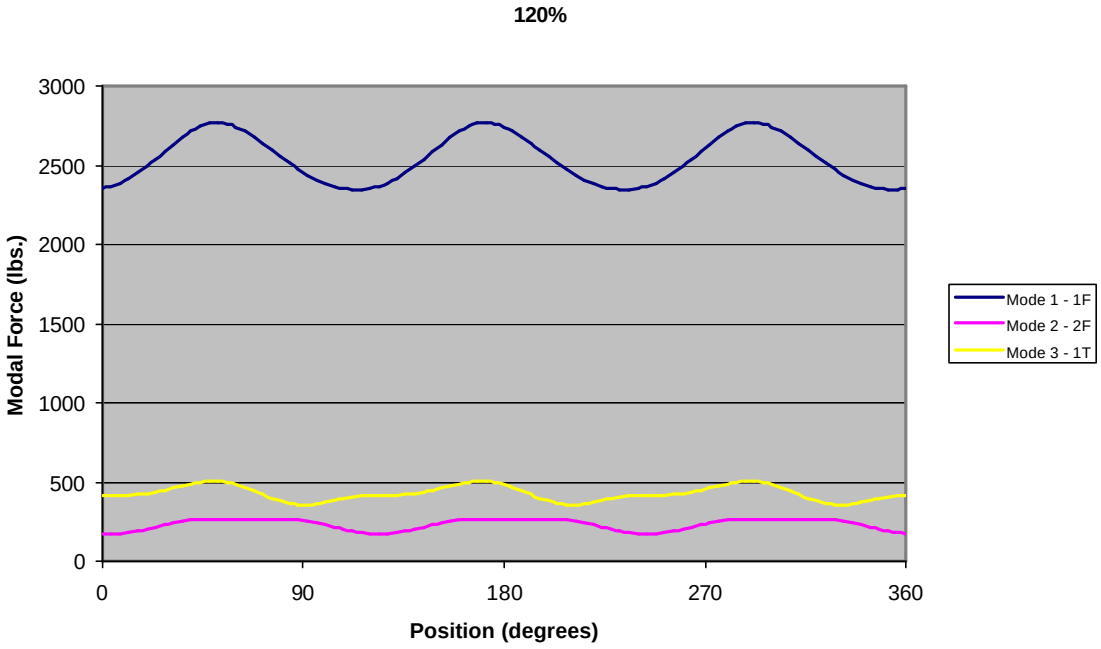

Figure 5-9: Modal force comparison at the 120% distortion level.

The results have been divided and displayed with respect to the two main categories in which to analyze the data, first by mode and second by inlet distortion level. When inspecting the plots arranged by mode, two things should be noted. First, the average value at which the generalized forcing function oscillates about, and second, the amplitude of the forcing function. The average value indicates the baseline loading the blade undergoes while under the 3-per-rev distortion pattern with respect to its contribution towards exciting that particular mode. The amplitude of the oscillation shows how much the loading changes as a result of the sinusoidal excitation. It is important to remember that the only thing changing between the separate modal plots are the eigenvectors associated with that mode; the pressure vectors used in the inner product remain the same throughout the analyses. As expected, the amplitude for each mode changes with the distortion level present and the shape of the sinusoidal generalized forcing function changes in accordance with the mode shape.

The second set of plots holds the distortion level constant for each plot while each of the three modes is plotted for each distortion level. These plots are a better indication of the difference in average blade loading caused by the 3-per-rev pressure distortion with respect to the contribution towards each mode. To better understand the idea of the same distortion pattern and level contributing different amounts to the three mode shapes, consider an example of a diving board.

Like a diving board, the compressor blade being studying is essentially a flat plate cantilevered on one end. Consider a person standing on the end of the diving board, and for now, think of the pressure loading on the blade only acting through one point as a single force. The person's weight will cause the board to deflect a finite amount dependant on the geometry and material properties of the diving board. Now consider the person jumping up and down on the board in such a way that their feet never lose contact with the board surface and every time their weight is exerted back on the board, the board is already moving downward, so the force they exert is always in the same direction of motion. It's easy to see in this way that the average deflection of the board as well as the amplitude of the oscillations could be large. This is exactly the scenario the blade will experience during the 1^{st} mode, called 1^{st} flexural. Now, to understand why the average deflection of the 2^{nd} and 3^{rd} mode is much less, you need to superimpose the

motion of the person jumping on the board onto a picture of the board deflecting in a different manner. Choosing the 3rd mode, called 1st torsional, the board will be twisted as if someone at the end of the board grasps both sides and applies a torque clockwise, and then counterclockwise over and over again. How much of the energy applied by the person jumping on the board helps this torque accomplish its deflection mode of twisting the board? When twisted, half of the board is moving downward while the other half is moving upward, so part of the energy exerted by the jumping person helps the side going downward, yet opposes the side going upward. If the blade were symmetric like a diving board, the effect would cause each side to cancel the other side out, however the blade is not symmetric and therefore a nonzero contribution exists. However, as expected, the 1st mode generalized forcing function is many times higher than the 2nd and 3rd mode since the oscillating pressure on the blade coincides with the natural motion of the blade in 1st flexural.

5.3 Fast Fourier Transform of the Generalized Forcing Function

A Fast Fourier Transform (FFT) was conducted on the generalized forcing function in order to determine the harmonic decomposition of the function. The modal force amplitudes have been plotted and appear in Figure 5-10 through Figure 5-12.

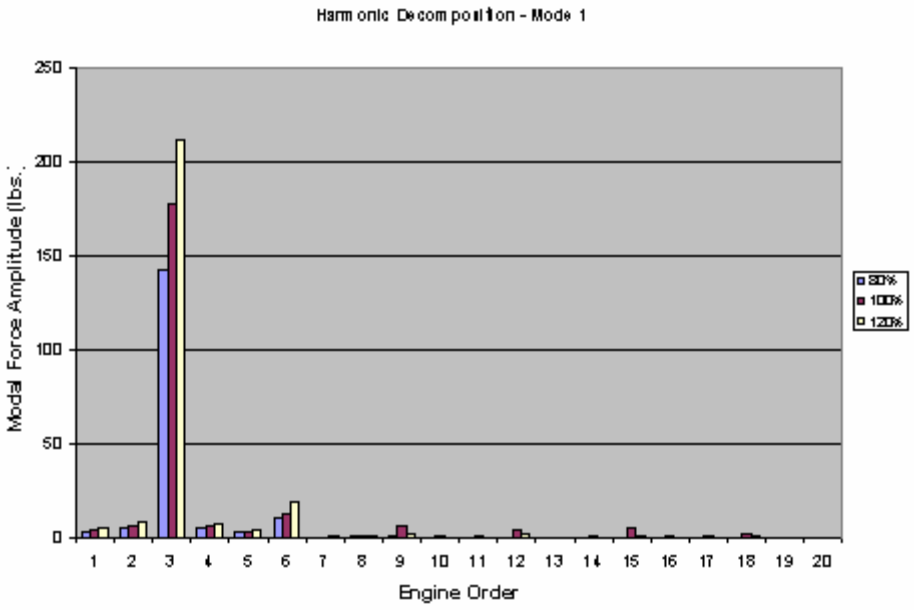

Figure 5-10: Harmonic content present in the 1st mode.

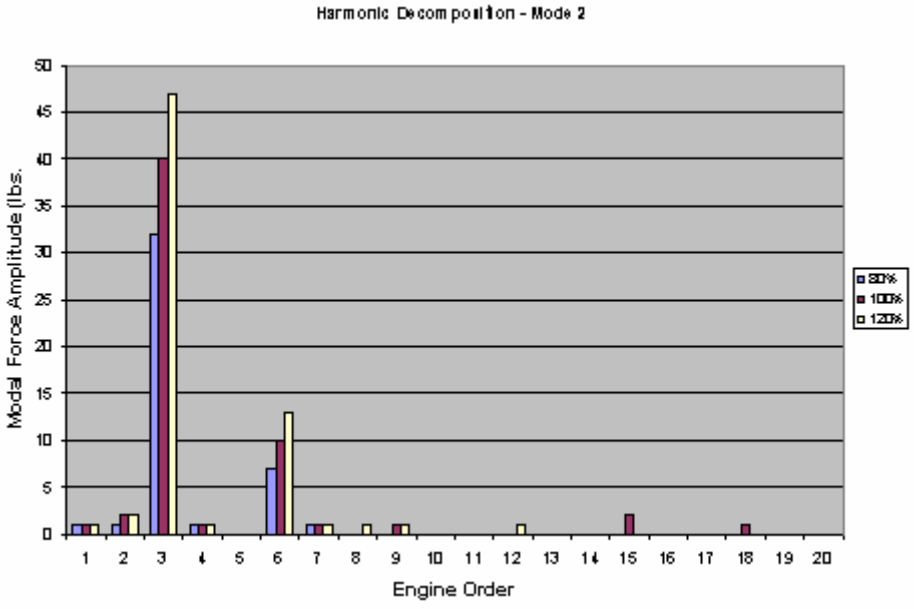

Figure 5-11: Harmonic content present in the 2nd mode.

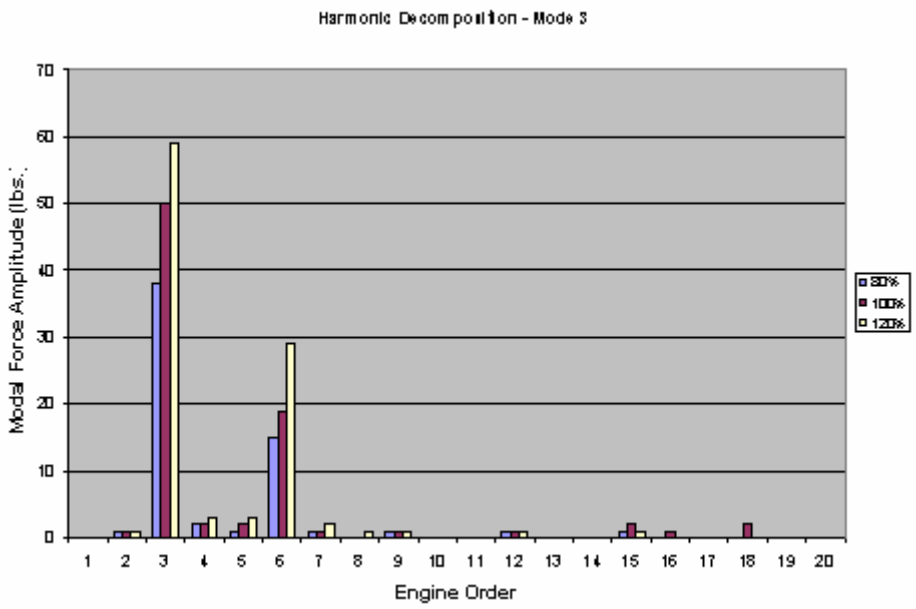

Figure 5-12: Harmonic content present in the 3rd mode.

The x-axis is labeled as Engine Order to denote the number of excitations per revolution and therefore it is no surprise again to see the highest modal force is present at the 3rd engine order. The zero engine order represents a DC offset, which corresponds to the average baseline blade loading discussed earlier. This value is so much larger than the oscillation magnitudes that it has been eliminated to make better use of plot scale. In addition, the amplitude of the oscillations is of greater importance than the baseline blade loading as this is the driver of high cycle fatigue. The modal force results from the FFT indicate how much of the amplitude present in the sinusoidal forcing function is a result of the various engine orders. The second highest modal force amplitude present was the 6th engine order, a harmonic of the 3rd engine order. In the 3rd mode this 6th engine order response was quite high and can actually be seen as a smaller extra "peak" or area where the sinusoid plateaus between the major trough and peak of the sinusoid in Figure 5-6.

A table summarizing the modal force amplitude of the 3rd engine order and the 6th engine order has been included as Table 5-2 for each mode and distortion level. The first mode has been highlighted as it had the highest modal force.

Table 5-2: Modal force summary.

Mode	3rd EO (lbs)	6th EO (lbs)	Level
1	142	10	80%
1	177	13	100%
1	211	19	120%
2	32	7	80%
2	40	10	100%
2	47	13	120%
3	38	15	80%
3	50	19	100%
3	59	29	120%

5.4 Sensitivity Analysis

In an attempt to easily determine the relationship between the level of inlet pressure distortion and the modal force amplitude of the various modes tested, a sensitivity plot was developed. A plot for the 3rd and 6th engine order have been included as Figure 5-13 and Figure 5-14, respectively.

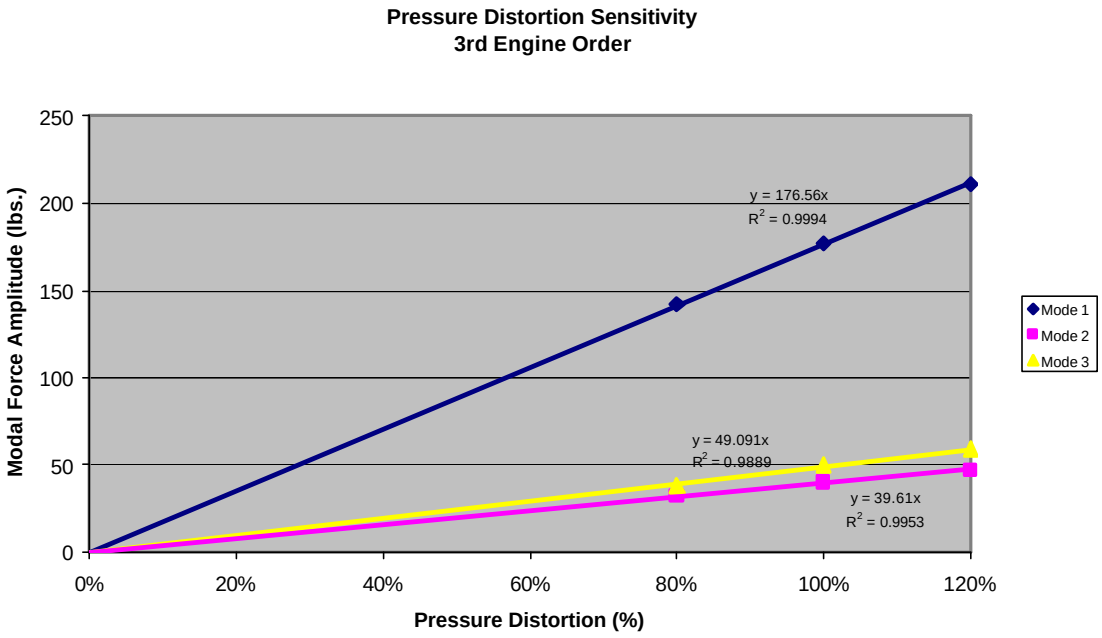

Figure 5-13: 3rd Engine order pressure distortion sensitivity.

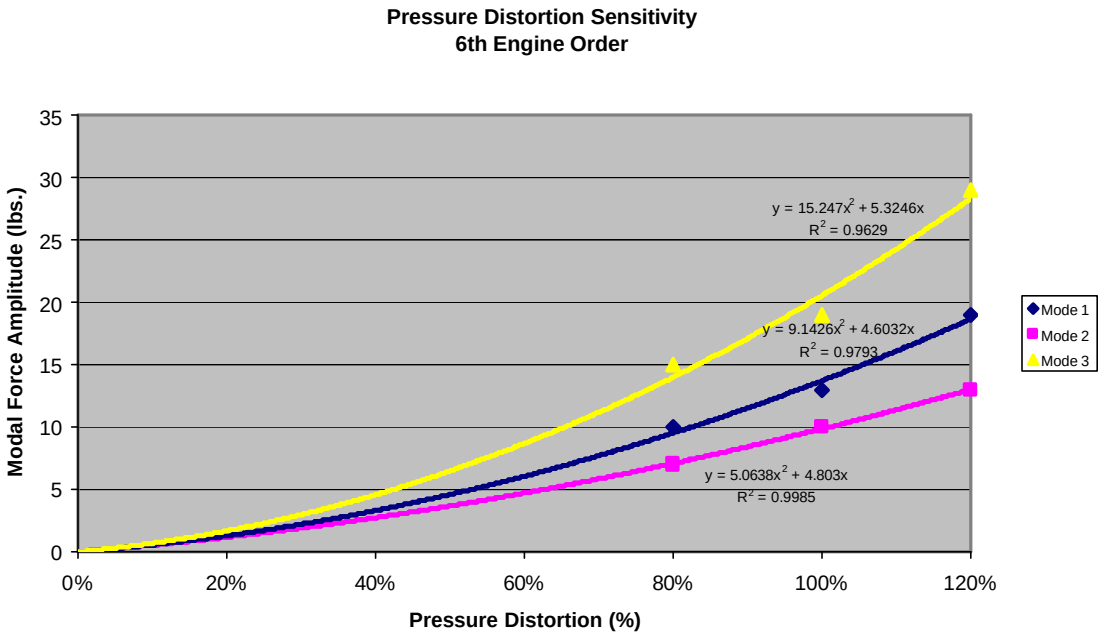

Figure 5-14: 6th Engine order pressure distortion sensitivity.

In Figure 5-13 it can be seen that the relationship between the modal force amplitude and the pressure distortion level appears to be very linear. A best fit line has been added with the equation and R^2 value included. The equation was forced through zero in the assumption that there should be no force present in the absence of any pressure distortion. The slope of the line indicates the sensitivity factor. The sensitivity factor indicates the gain in modal force as a function of percent gain in total pressure distortion. For example, for the 1st mode a 20% increase in total pressure distortion results in a 176.6 x 20% = 35.3 gain in modal force. The 6th engine order sensitivity factor plot was made to see the relationship between pressure distortion and modal force for an engine order that was a harmonic of the engine order being directly excited by the distortion screen. From Figure 5-14 it appears that the relationship may be parabolic as the R^2 values are still relatively high with the equations being forced through zero once again. It is important to realize that the pressure distortion amplitudes are nonlinear for these harmonics and the sensitivity depends on the pressure distortion amplitude. However, for both plots the available data is limited with only three data points and adding a forth by forcing it through zero. It is often dangerous and possibly misleading to extrapolate over a large area as is done here but for the data points available, the R^2 value seem to indicate a good fit, especially in the linear case for the 3rd engine order. A sensitivity factor summary is shown in Table 5-3.

Table 5-3: Sensitivity factor summary.

	Mode 1	**Mode 2**	**Mode 3**
3rd EO	176.6(x)	39.6(x)	49.1(x)
6th EO	30.5(x) + 5.3	10.1(x) + 4.8	18.3(x) + 4.6

5.5 Checking Modal Force Results with Strain Gage Data

During initial testing of the ADLARF compressor at the CRF, three strain gages were placed at various locations on the suction side of the fan blade to measure response of strain and therefore stresses present. Twenty seconds of recorded data for resonant

operation at 8100 rpm and 9100 rpm were sampled at a rate of 2.5 kHz [Kenyon, 1999]. A diagram showing the location of the three strain gages is shown in Figure 5-15.

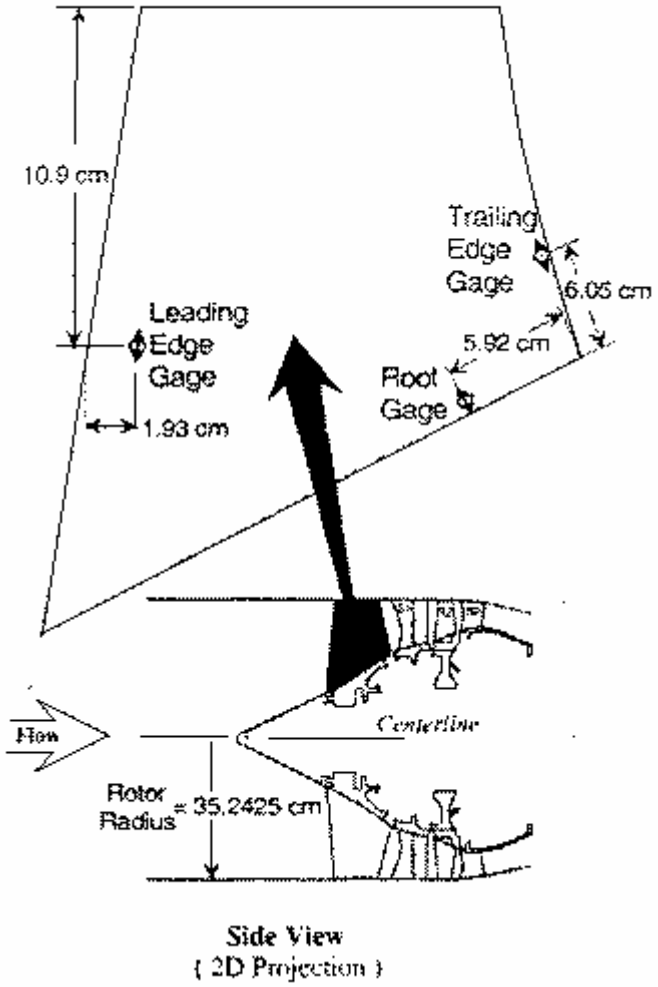

Figure 5-15: Side view of the test compressor showing strain gage location [Kenyon, 1999].

The Root Gage was located 5.92 cm from the trailing edge of the blade, which corresponds to Node 47 along the base of the blade. The strain gage however covers a small area just above the blade root and so the Node 177 located 2 elemental rows, approximately ¼ inches, above the root was chosen to compare stresses with experimental values found. The blade root was not aligned with any of the three axes in Ansys and therefore a direct output from one of Ansys' predetermined directions aligned

with the coordinate system was not possible. A vector describing the direction and location of the strain gage had to be determined as components in the x, y, and z directions. Again, Tecplot was employed to find this vector by outputting a vector normal to a slice through the blade at the strain gage location. This resulted in a unit vector of -0.551769, -0.057844, and 0.831988 in the x,y, and z directions, respectively. These vectors were then multiplied by stresses found in the way described in the following section.

In order to apply the generalized forcing function onto the FE model in Ansys, a point had to be chosen and then the appropriate force had to be determined. Any point will work equally well as the force changes depending on the location chosen. A point was arbitrarily chosen, Node 1887, which is one node back from the leading edge tip on the suction side of the blade. At this location the magnitude of the eigenvector was 45.000. To find the correct force to apply, the generalized force is simply divided by the displacement for the mode of interest. In this case the 1st mode is used since this is the mode being excited in the experimental stress data used for comparison. The equation and solution appear below.

$$\tilde{\Phi}_1^T \tilde{f}_1 = \tilde{\Phi}_2^T \tilde{f}_2$$

Equation 5-12

$$F_1 = \tilde{\Phi}_2^T \tilde{f}_2$$

let $x_2 = \tilde{\Phi}_2$ at a chosen point,

and let f_2 be a point force so that,

$$F_1 = x_2 f_2$$

$$\therefore f_2 = \frac{F_1}{x_2}$$

$$f_2 = \frac{177 lbs.}{45} = 3.933 lbs.$$

The variables f_1 and F_1 represent the total modal force and the eigenvector respectively, while f_2 and F_2 represent the modal force and eigenvector at a specific point. The force of 3.933 lbs. was applied at Node 1887 along the direction of eigenvector and was varied harmonically. The harmonic variance of the force is used so that the maximum stress can be determined as the force oscillates from zero to its maximum while slowly increasing in frequency. As the frequency at which the force is applied sweeps past the natural frequency of the blade, the deflection, strain and stress all reach their maximums. A plot showing the maximum stress present at the strain gage location in the x, y, and z directions are shown below in Figure 5-16 through Figure 5-18, respectively.

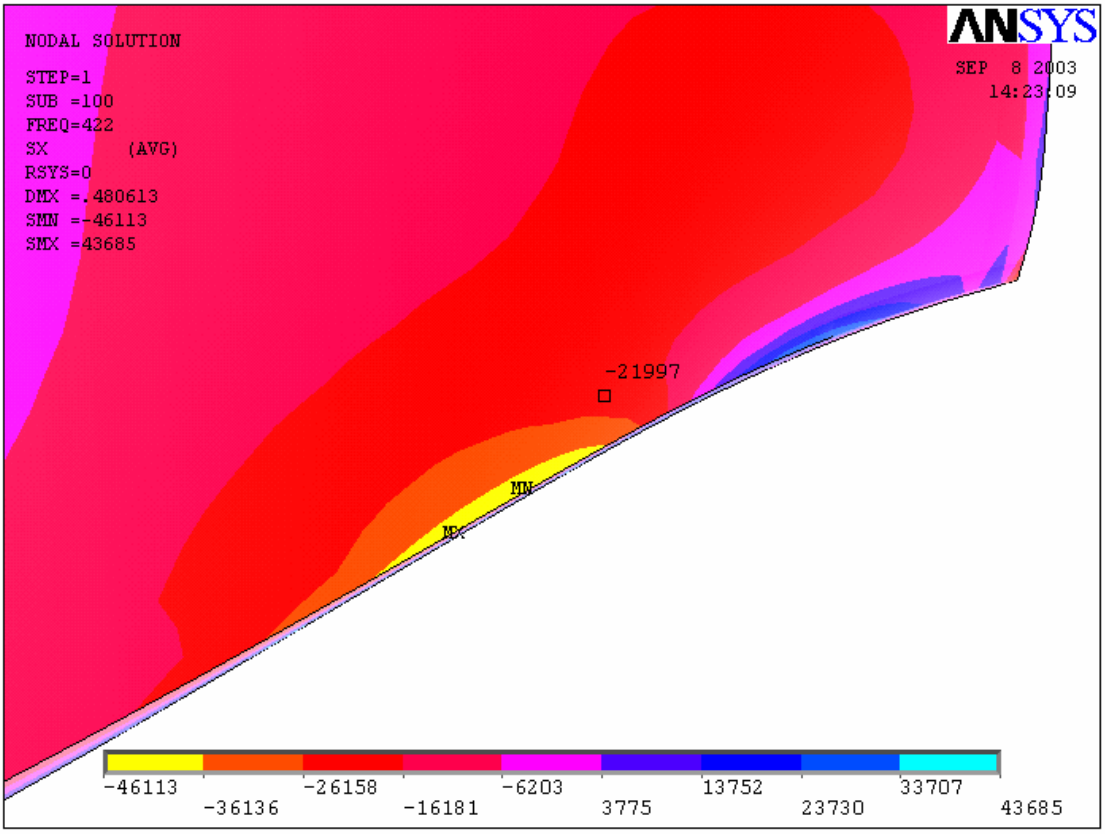

Figure 5-16: Blade root stress in the x-direction.

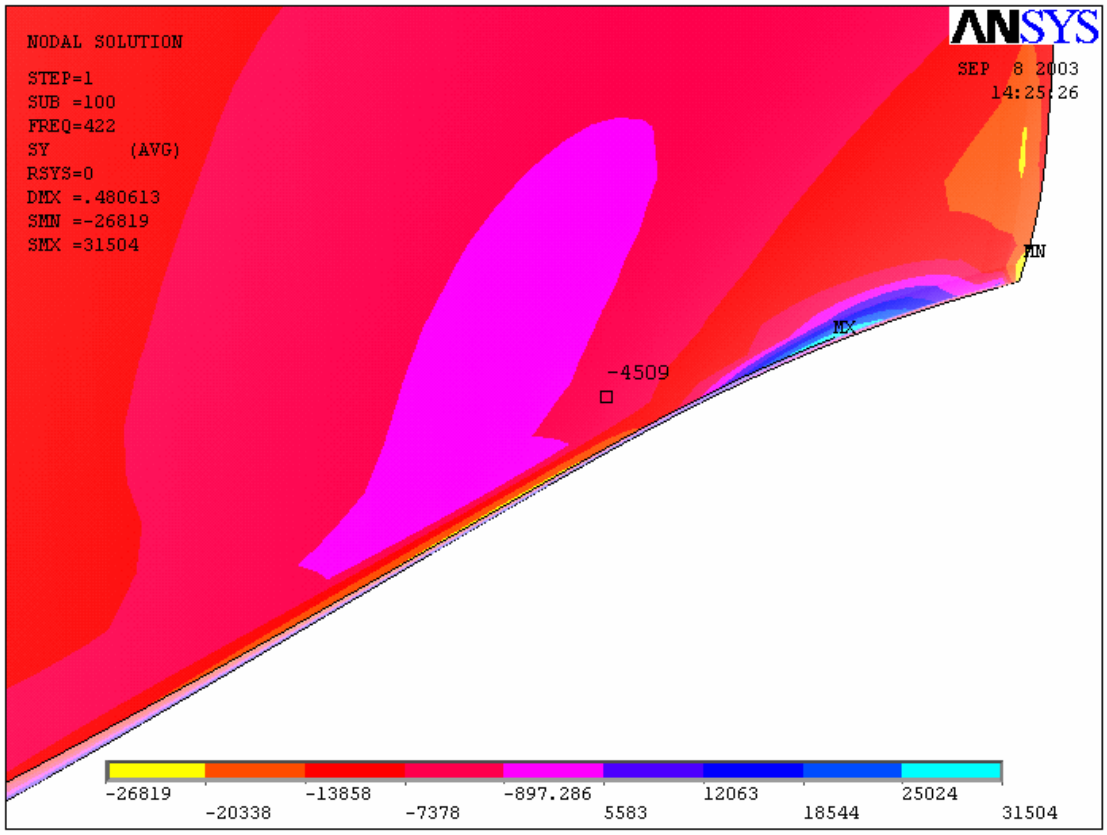

Figure 5-17: Blade root stress in the y-direction.

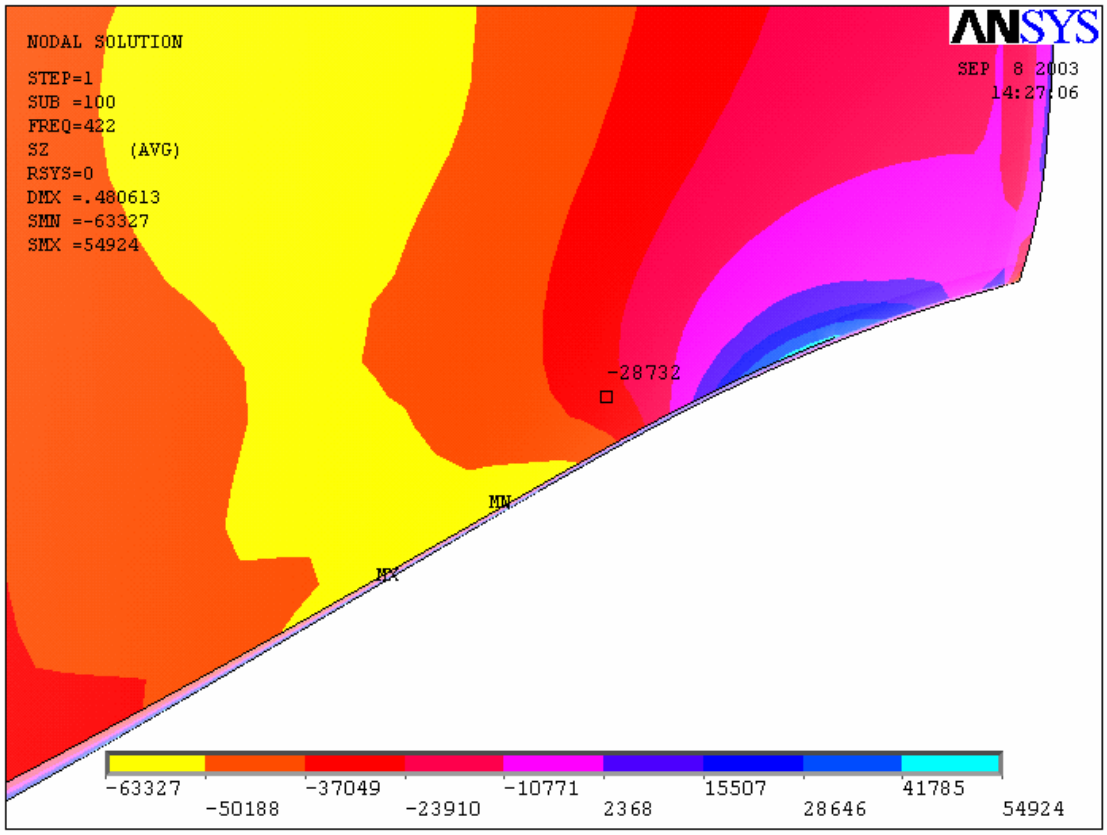

Figure 5-18: Blade root stress in the z-direction.

The rotor mean resonant stress found experimentally was 145,335 kPa [Kenyon, 1999]. The stress found using the FE model for the harmonic analysis resulted in a stress of -21997, -4509, and -28732 psi for pure titanium and –19740, -4069, and -25764 for Ti-6-4 in the x, y, and z direction, respectively. Once the stresses have been multiplied by the unit vector describing the strain gage orientation, the results must be doubled to be consistent with the experimental results as reported by Kenyon to represent the total stress magnitude from the minimum to maximum (peak-to-peak). Table 5-4 shows the calculation of the individual contributions from each principle stress direction and summarizes the results.

Table 5-4: Mean rotor stress calculation and comparison at wide open discharge.

	FEM Stress (psi) (Ti-6-4)	Strain Gage Unit Vector	Contribution to Strain Gage (psi)
x	-19740	-0.551769	10891.9
y	-4069.6	-0.057844	235.4
z	-25763.6	0.831998	-21435
Total			-10307.7

Experimental Stress Results	FEM Stress Results	Percent Difference
21,132 psi	20,615 psi (Ti-6-4)	-2.51 %
	23,013 psi (Ti)	+8.18 %
145,335 kPa	141,783 kPa (Ti-6-4)	-2.51 %
	158,274 kPa (Ti)	+8.18 %

The results have been reported in both English and metric units since my work was done in English units and the experimental values were published in metric. The results show an agreement around 2.5%, this is an extremely good result and indicates that the simple model was able to accurately predict blade root stress using relatively inexpensive computations. In addition, the experimentally found blade root stress varied up to 21% of the mean near stall with a standard deviation of 9.8% at wide-open discharge [Kenyon, 1999]. Given this uncertainty in the experimental results, the FE stress result of 2.51% from the mean stress is well within one standard deviation.

6 Summary and Conclusions

The ability of modal analysis to accurately predict blade loading in a transonic axial compressor has been investigated. A method and parametric model has been developed using modal analysis with a harmonically varying excitation to predict the strain and stress in a finite element model. This method is based on calculating and extracting the eigenvectors associated with a finite element model and combining them with a known pressure profile created with computational fluid dynamics on the same blade grid. An inner product was taken between the pressure profile and three different mode shapes: 1st Flexural, 2nd Flexural, and 1st Torsional. These mode shapes represent the first three modes associated with the three lowest natural frequencies present in the compressor blade under the operating conditions. The lowest order mode shapes contain the largest amount of energy resulting in large deflections and therefore inducing the highest strain and stress leading to possible high cycle fatigue.

Second, a generalized forcing function was computed as the inner product was calculated over time. The forcing function was plotted for all three modes over time to visually inspect and compare how each mode was excited by the single 3-per-rev distortion pattern. As expected the first mode showed the highest average modal force and amplitude. A Fast Fourier Transform was taken of the generalized forcing function to decompose the sinusoidal signal into harmonic components and investigate their contribution to the entire signal. As expected the 3rd engine order returned the highest magnitude while a harmonic at the 6th engine order was second highest contributing a significant portion for the 3rd mode – 1st Torsional.

A sensitivity factor was developed to show the gain in modal force as a function of percent gain in total pressure distortion. A linear relationship appears to exist for the 3rd engine order which each mode having a different sensitivity. The 1st mode has the highest gain in modal force for a given increase in total pressure distortion level followed by the 3rd mode and last the 2nd mode. The 6th engine order appears to have a parabolic relationship indicating the gain in modal force increases at an increasing rate as the level of the total pressure distortion increases.

To verify the accuracy of the modal analysis and to predict the strain and stress in the compressor blade, a harmonic analysis was conducted. Using the modal force calculated, a point force was determined on an arbitrarily picked node on the finite element model. This point force was placed on the blade node acting in the same direction as given by the 1st mode eigenvector and varied harmonically from zero to its maximum magnitude. This harmonic sweep was conducted over the frequency range known to contain the natural frequency of the blade associated with the first mode in an attempt to acquire the maximum strain and stress. Without the harmonic sweep, the exact natural frequency would need to be known in order to apply the force at the identical frequency. A node on the FE model was chosen that coincided with location of the rotor blade root strain gage in which stress was sampled and compared with the experimentally found value. The strain gage orientation required a stress to be calculated using components of the stress in all of the x, y, and z directions. This was done and the stress was found to be within 2.51% of the experimental value.

The model contained a few approximations and assumptions that strengthen the argument of this approach to accurately model and predict blade loading. The preliminary model used the density and modulus of elasticity of pure titanium instead of the actual titanium alloy, Ti-4-6, used in the blade. The difference resulted in a modulus of elasticity deficit of 10.3% with a gain in density of 8.2% in the model. Despite these deviations in material properties from Ti-6-4, the model still predicted blade root stress to within 8.18% found experimentally. The only available blade geometry was that used in the CFD calculations. This hot geometry was in the form of a finite element grid with a density of 64 by 29 elements, in the streamwise and spanwise direction, respectively. An internal element thickness of 3 elements was added along the primary axis of bending for accuracy in accordance with Ansys element definition suggestions. A cold geometry would have been preferred so the proper artificial stiffening due to centrifugal force and blade geometry at engine operation speed due to untwist could have been achieved simultaneously. As a result, the hot geometry was tested to see if the correct eigenvectors could be extracted and was found that it could. The maximum RMS error of 0.9289% was found and considered to be minimal, therefore allowing the eigenvectors to be extracted from the hot geometry while spinning at 9100 rpm. This allowed

approximately the correct eigenvalues and eigenvectors to be present in the model simultaneously.

The goals of this particular study were introduced in Chapter 1 and will be re-iterated here: (1) create an accurate finite element (FE) model of the ADLARF fan blade for eigenvector extraction; (2) identify dominant engine order modal force magnitudes based on coupling computational fluid dynamics (CFD) generated total pressure distortion and FE generated eigenvectors; and (3) determine the relationship between the magnitude of the modal force and the total pressure distortion level used to drive the system. The goals have been achieved here for the 1^{st} mode – 1^{st} Flexural conditions as dictated by the available data. Many approximations and assumptions were taken along the way and go to show the ability of modal analysis to accurately predict the blade loading to within 2.51% despite these assumptions and approximations. This result is extremely good and falls within one standard deviation of the experimentally found blade root stress. This study is in conjunction with previous studies conducted by Jon Ludke and John Ryman at Virginia Tech to determine if pressure distortions continue through multiple stages of an axial compressor. Their studies show that the pressure distortions do in fact travel downstream and underline the importance of developing a method to predict blade loading as the possible problems associated with high cycle fatigue can not be assumed to be limited to the first stage rotor. This study has shown one possible method by developing a parametric model to determine blade loading sensitivity to varying total pressure distortions and predicting the strain and stress at the blade root as a result of forced vibration.

7 Recommendations for Future Work

This study has shown that it is possible to accurately predict the root strain and stress present in an axial compressor blade through modal analysis. While the results appear promising, the study was conducted with limited data taken at only one distortion pattern and one engine operation speed. More research should be conducted using additional compressor blades, inlet distortion patterns, and engine operation speeds before a complete picture of the ability of modal analysis to accurately predict the strain and stress can be commented upon and implemented in industry to partially eliminate the arduous task of testing.

The next step in testing should be the use of total temperature distortions at the inlet. Since temperature and pressure are directly related through the Ideal Gas Law it is believed that modal analysis could be used to analyze the effect of total temperature change in the same way total pressure was tested. There has been much discussion in the industry lately as to whether total temperature distortion can produce excitations capable of inducing high cycle fatigue. This study may introduce one of many avenues to investigate this topic of debate.

In addition, if further testing proves promising using this parametric method of testing blade loading to inlet distortions that are quasi-steady state, perhaps a method of introducing unsteady inlet distortions could be investigated. Studies by Jon Ludke and John Ryman at Virginia Tech have shown that total pressure distortions pass through multiple rotor rows in an axial compressor. As a result, perhaps this method can be combined with their studies to predict blade loading on rotor blades farther downstream. Ultimately the model developed here may be expanded to study many other systems where forced vibrations are present and if the application continues to be successful could reach areas of interest far outside the realm of turbomachinery.

Appendix

Preliminary Matlab FE Code

```
function [eigenvectors] = Eigenvalue_solver( ae, ei, l, deg1, deg2, rho, Asec, rpm );
% ME5634FE_2DBeamStaticStiffness - Compute 2-D Beam Element Static Stiffness Matrix
%
%*************************************************************************
%
%   Function:  2 Element Frame Eigenvalue Solver
%
%
%   Description:  Computes the element static stiffness matrix, mass matrix,
%                 and eigenvalues for a 2-D frame-type element.
%
%
%   Calling Sequence:
%
%   ke = ME5634FE_2DBeamStaticStiffness ( ae, ei, l, deg1, deg2, mbar )
%
%   Input:   ae  - product of elastic modulus * cross-section area
%            ei  - product of elastic modulus * area moment of inertia
%            l   - element length
%          deg1  - angle first element makes with horizontal in degrees
%          deg2  - angle first element makes with horizontal in degrees
%          rho   - density
%          Asec  - cross sectional area
%          rpm   - rotational speed in revolutions per minute
%
%   Output:  ke - 2-D frame element stiffness matrix
%
%
%   Rev   Date      Name                Version
%     - Description:
%   00  24-Mar-03   Rob Wallace           0.0
%
%*************************************************************************

l2 = l * l;                     % compute l squared
l3 = l2 * l;                    % compute l cubed

k   = ae / l;                   % compute axial stiffness

theta1 = deg1*pi/180;           % convert degrees to radians
theta2 = deg2*pi/180;           % convert degrees to radians

mbar = rho*Asec;                % computes distributed mass number

mm = mbar*l/420;                % mass multiplier

omega = rpm*2*pi/60;            % converts rpm to rad/s
```

```
k11 =  k;
k12 = 0.0;
k13 = 0.0;
k14 = -k;
k15 = 0.0;
k16 = 0.0;

k21 = k12;
k22 =  12 * ei / l3;
k23 =   6 * ei / l2;
k24 = 0.0;
k25 = -k22;
k26 =  k23;


k31 =  k13;
k32 =  k23;
k33 =   4 * ei / l;
k34 =  0.0;
k35 = -k32;
k36 =   2 * ei / l;

k41 =  k14;
k42 =  k24;
k43 =  k34;
k44 =  k11;
k45 =  0.0;
k46 =  0.0;

k51 =  k15;
k52 =  k25;
k53 =  k35;
k54 =  k45;
k55 =  k22;
k56 =  k53;

k61 =  k16;
k62 =  k26;
k63 =  k36;
k64 =  k46;
k65 =  k56;
k66 =  k33;

% now use symmetry to build the static stiffness matrix
ke1i = [ k11, k12, k13, k14, k15, k16;  ...                % Element 1 stiffness matrix, local coordinates
       k21, k22, k23, k24, k25, k26;  ...
       k31, k32, k33, k34, k35, k36;  ...
       k41, k42, k43, k44, k45, k46;  ...
       k51, k52, k53, k54, k55, k56;  ...
       k61, k62, k63, k64, k65, k66 ];


ke2i = [ k11, k12, k13, k14, k15, k16;  ...                % Element 2 stiffness matrix, local coordinates
       k21, k22, k23, k24, k25, k26;  ...
       k31, k32, k33, k34, k35, k36;  ...
```

```
    k41, k42, k43, k44, k45, k46;  ...
    k51, k52, k53, k54, k55, k56;  ...
    k61, k62, k63, k64, k65, k66 ];


angle1 = [ cos(theta1), sin(theta1), 0, 0, 0, 0; ...          % Element 1 transformation matrix to global
coordinates
     -sin(theta1), cos(theta1), 0, 0, 0, 0; ...
     0, 0, 1, 0, 0, 0; ...
     0, 0, 0, cos(theta1), sin(theta1), 0; ...
     0, 0, 0, -sin(theta1), cos(theta1), 0; ...
     0, 0, 0, 0, 0, 1 ];


angle2 = [ cos(theta2), sin(theta2), 0, 0, 0, 0; ...          % Element 2 transformation matrix to global
coordinates
     -sin(theta2), cos(theta2), 0, 0, 0, 0; ...
     0, 0, 1, 0, 0, 0; ...
     0, 0, 0, cos(theta2), sin(theta2), 0; ...
     0, 0, 0, -sin(theta2), cos(theta2), 0; ...
     0, 0, 0, 0, 0, 1 ];

ke1 = [angle1]'*[ke1i]*[angle1];          % Transforming element 1 stiffness matrix to global coordinates
ke2 = [angle2]'*[ke2i]*[angle2];          % Transforming element 2 stiffness matrix to global coordinates


ket = [ ke1(1,1), ke1(1,2), ke1(1,3), ke1(1,4), ke1(1,5), ke1(1,6), 0, 0, 0; ...    %Combined global stiffness
matrix
    ke1(2,1), ke1(2,2), ke1(2,3), ke1(2,4), ke1(2,5), ke1(2,6), 0, 0, 0; ...
    ke1(3,1), ke1(3,2), ke1(3,3), ke1(3,4), ke1(3,5), ke1(3,6), 0, 0, 0; ...
    ke1(4,1), ke1(4,2), ke1(4,3), ke1(4,4)+ke2(1,1), ke1(4,5)+ke2(1,2), ke1(4,6)+ke2(1,3), ke2(1,4),
ke2(1,5), ke2(1,6); ...
    ke1(5,1), ke1(5,2), ke1(5,3), ke1(5,4)+ke2(2,1), ke1(5,5)+ke2(2,2), ke1(5,6)+ke2(2,3), ke2(2,4),
ke2(2,5), ke2(2,6); ...
    ke1(6,1), ke1(6,2), ke1(6,3), ke1(6,4)+ke2(3,1), ke1(6,5)+ke2(3,2), ke1(6,6)+ke2(3,3), ke2(3,4),
ke2(3,5), ke2(3,6); ...
    0, 0, 0, ke2(4,1), ke2(4,2), ke2(4,3), ke2(4,4), ke2(4,5), ke2(4,6); ...
    0, 0, 0, ke2(5,1), ke2(5,2), ke2(5,3), ke2(5,4), ke2(5,5), ke2(5,6); ...
    0, 0, 0, ke2(6,1), ke2(6,2), ke2(6,3), ke2(6,4), ke2(6,5), ke2(6,6) ];

mass = mm * [ 140, 0, 0, 70, 0, 0; ...                    %General distributed mass matrix, local coordinates
     0, 156, 22*1, 0, 54, -13*l; ...
     0, 22*l, 4*l2, 0, 13*l, -3*l2; ...
     70, 0, 0, 140, 0, 0; ...
     0, 54, 13*l, 0, 156, -22*l; ...
     0, -13*l, -3*l2, 0, -22*l, 4*l2 ];

mass1 = [angle1]'*[mass]*[angle1];          % Transforming element 1 mass matrix to global coordinates
mass2 = [angle2]'*[mass]*[angle2];          % Transforming element 2 mass matrix to global coordinates


masst = [ mass1(1,1), mass1(1,2), mass1(1,3), mass1(1,4), mass1(1,5), mass1(1,6), 0, 0, 0; ...  %Combined
global mass matrix
    mass1(2,1), mass1(2,2), mass1(2,3), mass1(2,4), mass1(2,5), mass1(2,6), 0, 0, 0; ...
    mass1(3,1), mass1(3,2), mass1(3,3), mass1(3,4), mass1(3,5), mass1(3,6), 0, 0, 0; ...
```

```
      mass1(4,1), mass1(4,2), mass1(4,3), mass1(4,4)+mass2(1,1), mass1(4,5)+mass2(1,2),
mass1(4,6)+mass2(1,3), mass2(1,4), mass2(1,5), mass2(1,6); ...
      mass1(5,1), mass1(5,2), mass1(5,3), mass1(5,4)+mass2(2,1), mass1(5,5)+mass2(2,2),
mass1(5,6)+mass2(2,3), mass2(2,4), mass2(2,5), mass2(2,6); ...
      mass1(6,1), mass1(6,2), mass1(6,3), mass1(6,4)+mass2(3,1), mass1(6,5)+mass2(3,2),
mass1(6,6)+mass2(3,3), mass2(3,4), mass2(3,5), mass2(3,6); ...
      0, 0, 0, mass2(4,1), mass2(4,2), mass2(4,3), mass2(4,4), mass2(4,5), mass2(4,6); ...
      0, 0, 0, mass2(5,1), mass2(5,2), mass2(5,3), mass2(5,4), mass2(5,5), mass2(5,6); ...
      0, 0, 0, mass2(6,1), mass2(6,2), mass2(6,3), mass2(6,4), mass2(6,5), mass2(6,6) ];


ac1=0;
ac2=0;

 for i = 4:9                                  % Eliminating rows/columns due to model contraints
    ac1 = ac1 + 1;
    for j = 4:9
       ac2 = ac2 + 1;
       cmass(ac1,ac2) = masst(i,j);
       cket(ac1,ac2) = ket(i,j);
    end
    ac2 = 0;
 end

eigenvectors = eig(cket,cmass);                    % Computes the eigenvalues for the model

for m = 1:6                                   % Converts the eigenvalues to natural frequencies in Hz
nat_freq_Hz_unspun(m,1) = (((eigenvectors(m,1))^(1/2))/(2*pi));
end

nat_freq_Hz_unspun


F1 = (64*rho*omega^2)/(3*l);
F2 = ((8-(64/(3*l)))*rho*omega^2)+((448/(3*l))*rho*omega^2);
F3 = (24-(448/(3*l)))*rho*omega^2;

F12 = (F1+F2)/2;
F23 = (F2+F3)/2;


Psk1 = F12/l * [0, 0, 0, 0, 0, 0; ...
             0, 6/5, l/10, 0, -6/5, l/10; ...
             0, l/10, 2*l2/15, 0, -l/10, -l2/30; ...
             0, 0, 0, 0, 0, 0; ...
             0, -6/5, l/10, 0, 6/5, -l/10; ...
             0, l/10, -l2/30, 0, -l/10, 2*l2/15];

Psk2 = F23/l * [0, 0, 0, 0, 0, 0; ...
             0, 6/5, l/10, 0, -6/5, l/10; ...
             0, l/10, 2*l2/15, 0, -l/10, -l2/30; ...
             0, 0, 0, 0, 0, 0; ...
             0, -6/5, l/10, 0, 6/5, -l/10; ...
             0, l/10, -l2/30, 0, -l/10, 2*l2/15];

Pske1i = [ke1i]+[Psk1];                          % Add prestress riser to element 1 stiffness matrix
```

```
Pske2i = [ke2i]+[Psk2];                          % Add prestress riser to element 2 stiffness matrix

ke1 = [angle1]'*[Pske1i]*[angle1];          % Transforming element 1 stiffness matrix to global coordinates
ke2 = [angle2]'*[Pske2i]*[angle2];          % Transforming element 2 stiffness matrix to global coordinates

ket = [ ke1(1,1), ke1(1,2), ke1(1,3), ke1(1,4), ke1(1,5), ke1(1,6), 0, 0, 0; ...    %Combined global stiffness
matrix
      ke1(2,1), ke1(2,2), ke1(2,3), ke1(2,4), ke1(2,5), ke1(2,6), 0, 0, 0; ...
      ke1(3,1), ke1(3,2), ke1(3,3), ke1(3,4), ke1(3,5), ke1(3,6), 0, 0, 0; ...
      ke1(4,1), ke1(4,2), ke1(4,3), ke1(4,4)+ke2(1,1), ke1(4,5)+ke2(1,2), ke1(4,6)+ke2(1,3), ke2(1,4),
ke2(1,5), ke2(1,6); ...
      ke1(5,1), ke1(5,2), ke1(5,3), ke1(5,4)+ke2(2,1), ke1(5,5)+ke2(2,2), ke1(5,6)+ke2(2,3), ke2(2,4),
ke2(2,5), ke2(2,6); ...
      ke1(6,1), ke1(6,2), ke1(6,3), ke1(6,4)+ke2(3,1), ke1(6,5)+ke2(3,2), ke1(6,6)+ke2(3,3), ke2(3,4),
ke2(3,5), ke2(3,6); ...
      0, 0, 0, ke2(4,1), ke2(4,2), ke2(4,3), ke2(4,4), ke2(4,5), ke2(4,6); ...
      0, 0, 0, ke2(5,1), ke2(5,2), ke2(5,3), ke2(5,4), ke2(5,5), ke2(5,6); ...
      0, 0, 0, ke2(6,1), ke2(6,2), ke2(6,3), ke2(6,4), ke2(6,5), ke2(6,6) ];


ac1=0;
ac2=0;

 for i = 4:9                                    % Eliminating rows/columns due to model contraints
    ac1 = ac1 + 1;
    for j = 4:9
        ac2 = ac2 + 1;
       cmass(ac1,ac2) = masst(i,j);
       cket(ac1,ac2) = ket(i,j);
    end
    ac2 = 0;
 end


eigenvectors = eig(cket,cmass);                  % Computes the eigenvalues for the model

for m = 1:6                                      % Converts the eigenvalues to natural frequencies in Hz
nat_freq_Hz_spun(m,1) = (((eigenvectors(m,1))^(1/2))/(2*pi));
end

nat_freq_Hz_spun
```

References

ANSYS, v.61, www.ansys.com.

Bielawa, R. L., "Rotary Wing Structural Dynamics and Aeroelasticity," AIAA Education Series, 1992.

Boyer, K.E., "An Improved Streamline Curvature Approach for Off-Design Analysis of Transonic Compression Systems," Ph.D. Dissertation, Virginia Polytechnic Institute and State University (Blacksburg, VA, 2001).

Breard, Imregun, Sayma, Vahdati, "An Integratied Time Domain Aerolasticity Model for the Prediction of Fan Forced Response Due to Inlet Distortion," *Journal of Engineering for Gas Turbine and Power*, Vol. 124, Janurary 2002, pp. 196.

Campbell, Wilfred, "Protection of Turbine Disk Wheels from Axial Vibration," *Proceedings of the Cleveland Spring Meeting*, ASME, May 1924.

Carnegie, W., "Vibrations of Rotating Cantilever Blading: Theoretical Approaches to the Frequency Problem Based on Energy Methods," *Journal of Mechanical Engineering Science*, Vol. 1, No. 3, 1959, pp. 235-240.

Carta, F.O., "Aeroelasticity and Unsteady Aerodynamics," *The Aerothermodynamics of Aircraft Gas Turbines Engines*, AFAPL-TR-78-52, pp.22-10--22-11.

Cramer, K.B., O'Brien, W.F., "Design of a Total Distortion Generator for Aircraft Engine Testing," M.S. Thesis, Virginia Polytechnic Institute and State University (Blacksburg, VA, 2002).

Colpin, J., Kool, P., "Experimental Study of an Axial Compressor Rotor Transfer Function with Non-Uniform Inlet Flow." ASME Paper No. 78-GT-69, Gas Turbine Conference and Products Show, April 9-13, 1978, London, England.

Danforth, C.D., "Distortion-Induced Vibration in Fan and Compressor Blading," *Journal of Aircraft*, vol. 12, no. 4, pp. 216-225, April 1975.

Datko Jr., J.T., O'Hara, J.A., "The Aeromechanical Response of an Advanced Transonic Compressor to Inlet Distortion," ASME 87-GT-189, 1987.

Davis, M., Hale, A., Beale, D., "An Argument for Enhancement of the Current Inlet Distortion Ground Test Practice for Aircraft Gas Turbine Engines," ASME 2000-GT-0505, 2000.

Dhar, V.B., “A Simple Finite Element for the Dynamic Analysis of Rotating Composite Beams,” M.S. Thesis, Virginia Polytechnic Institute and State University (Blacksburg, VA, 1990).

Fleeter, S., Jay, R.L., Bennett, W.A., “Rotor Wake Generated Unsteady Aerodynamic Response of a Compressor Stator,” ASME 78-GT-112, 1978.

Greitzer, E.M., “Upstream Attenuation and Quasi-Steady Rotor Lift Fluctuations in Asymmetric Flows in Axial Compresors,” ASME 73-GT-30, 1973.

Greitzer, E.M., Tan, C.S., Wisler, D.C., Adamczyk, J.J., Stazisar, A.J., “Unsteady Flows in Turbomachines: Where’s the Beef?,” *ASME Unsteady Flows in Aeropropulsions*, 1994, pp. 1-11.

Hah, C., Rabe, D.C., Sullivan, T.J., Wadia, A.R., “Effects of Inlet Distortion on the Flow Field in a Transonic Compressor Rotor,” *ASME Journal of Turbomachinery*, Vol. 120, April 1998, pp. 233-246.

Hamed, A., Numbers, K., “Inlet Distortion Considerations for High Cycle Fatigue in Gas Turbine Engine,” AIAA Paper 97-3364, AIAA 33rd Joint Propulsion Conference and Exhibit, July 6-9, 1997, Seattle, WA.

Inman, D.J., “Engineering Vibration,” 2nd Ed., New Jersey, Prentice Hall, Inc., 2001.

Kenyon, J.A., private communication, 2003

Kenyon, J.A., “Investigation of Curve Veering Using Computational and Experimental Techniques,” AIAA-99-1383.

Kenyon, J.A., Fleeter, S., Rabe, D.C., “Aerodynamic Effects on Blade Vibratory Stress Variations,” *Journal of Propulsion and Power*, Vol. 15, No. 5, September-October 1999, pp. 675-680.

Lecht, M., “Improvement of the Parallel Compressor Model by Consideration of Unsteady Blade Aerodynamics,” AGARD CP-400, 1986.

Lecht, M., Weyer, H. B., “On the Unsteady Aerodynamic Rotor Blade Loading in a Transonic Axial Flow Compressor with Unsteady State Inlet Distortion,” IUTAM Symposium on Aeroelasticity in Turbomachines, October 18-23, 1976, Paris.

Longley, J.P., Greitzer, E.M., “Inlet Distortion Effects in Aircraft Propulsion System Integration,” *Steady and Transient Performance Prediction of Gas Turbine Engines*, AGARD LS-183, May 1992.

Manwaring, S.R., Fleeter, S., "Inlet Distortion Generated Periodic Aerodynamic Rotor Response," ASME 89-GT-299, 1989.

Manwaring, S.R., Fleeter, S., "Forcing Function Effects on Rotor Periodic Aerodynamic Response," *Transactions of the ASME*, vol. 113, April 1991, pp. 312-319.

Manwaring, S.R., Rabe, D.C., Lorence, C.B., Wadia, A.R., "Inlet Distortion Generated Forced Response of a Low Aspect-Ratio Transonic Fan," *ASME Journal of Turbomachinery*, vol. 119, October 1997, pp. 665-676.

Matlab, v.6.1, www.mathworks.com.

Mazzawy, R.S., "Multiple Segment Parallel Compressor Model for Circumferential Flow Distortion," *ASME Journal of Engineering for Power*, April, 1977.

Morrow, P., "Detailed Test Plan for the Augmented Damping of Low Aspect Ratio Fans (ADLARF)," USAF Technology Branch Turbine Engine Division, WPAFB, March 1993.

Peacock, R.E., Overli, J., "Dynamic Internal Flows in Compressors with Pressure Maldistributed Inlet Conditions," AGARD CP-177, 46th P.E.P. Conference of AGARD, 1975, Monterey, CA.

Rabe, D., Bolcs, A., and Russler, P., "Influence of Inlet Distortion on Transonic Compressor Blade Loading," AIAA 95-2461, Presented at the 31st Joint Propulsion Conference and Exhibit, July 1995, San Diego, CA.

Rabe, D., Williams, C., and Hah, C., "Inlet Flow Distortion and Unsteady Blade Response in a Transonic Axial Compressor Rotor," ISABE 99-7297, 1999.

Reid, C., "The Response of Axial Flow Compressors to Intake Flow Distortion." ASME Paper No. 69-GT-29, 1969.

Roberts, F., Plourde, G.A., Smakula, F. "Insights into Axial compressor Response to Distortion," AIAA Paper No. 68-565, 1968.

Ryman, J.F., private communication, 2003

Ryman, J.F., O'Brien, W.F., "Prediction of Inlet Distortion Transfer Through the Blade Rows in a Transonic Axial Compressor," M.S. Thesis, Virginia Polytechnic Institute and State University (Blacksburg, Virginia, 2003.).

SAE Aerospace Information Report – 1419, *Inlet Total-Pressure-Distortion considerations for Gas-Turbine Engines*, (Warrendale, PA, Rev. A, 1999).

Sexton, M.R., O'Brien, W.F., "A Model for Dynamic Loss Response in Axial-Flow Compressors," ASME 81-GT-154, 1981.

Silva, W.A., "Identification of Linear and Nonlinear Aerodynamic Impulse Responses Using Digital Filter Techniques," AIAA 97-3712, Aug. 1997.

Silva, W.A., "Extension of a Nonlinear Systems Theory to General-Frequency Unsteady Transonic Aerodynamic Responses," AIAA 93-1590, Apr. 1993.

Small, M., "Improved Methods for Predicting the Effects of Inlet Flow Distortion on the Performance of Axial Flow Compressor," M.S. Thesis, Virginia Polytechnic Institute and State University (Blacksburg, Virginia, 2001.).

Tecplot, www.tecplot.com .

Thomson, W.T., "Theory of Vibration with Application," Prentice Hall, Inc. 1981.

Williams, C., "Turbine Engine Research Center Inlet Distortion Measurement," 4th National Turbine Engine High Cycle Fatigue Conference, 1999, Monterey, CA.

Vita

Robert M. Wallace

The author, son of Robert Ernest and Lydia Dianne Wallace, was born in 1979 in Radford, Virginia and spent the next 18 years growing up in Pulaski, Virginia. He attended high school at Pulaski County High School and the Southwest Virginia Governor's School for Science, Math and Technology. His decision to become an engineer led to his enrollment in Mechanical Engineering at Virginia Tech in the fall of 1997. Graduating from Virginia Tech in May of 2001, he decided to continue his education at Virginia Tech pursuing a Master of Science degree. In the fall of 2001, he began his graduate studies in Mechanical Engineering at Virginia Tech. Upon graduation he will be taking some well deserved time off and pursue flying before joining the work force.